Atmos. Chem. Phys. Discuss., 14, 1–49, 2014
www.atmos-chem-phys-discuss.net/14/1/2014/
doi:10.5194/acpd-14-1-2014

Atmospheric Chemistry and Physics Discussions
Open Access

Global investigation of the Mg atom and ion layers using SCIAMACHY/Envisat observations between 70 km and 150 km altitude and WACCM-Mg model results

M. Langowski[1], C. von Savigny[1,2], J. P. Burrows[1], W. Feng[3], J. M. C. Plane[3], D. R. Marsh[4], D. Janches[5], M. Sinnhuber[6], and A. C. Aikin[7]

[1]Institute of Environmental Physics (IUP), University of Bremen, Germany
[2]Institut für Physik, Ernst-Moritz-Arndt-Universität Greifswald, Germany
[3]School of Chemistry, University of Leeds, UK
[4]National Center for Atmospheric Research, Boulder, Colorado, USA
[5]Space Weather Lab, GSFC/NASA, USA
[6]Institut für Meteorologie und Klimaforschung – Atmosphärische Spurengase und Fernerkundung, KIT, Karlsruhe, Germany
[7]The Catholic University of America, Washington D.C., USA

Received: 19 December 2013 – Accepted: 9 January 2014 – Published:

Correspondence to: M. Langowski (martin.langowski@iup.physik.uni-bremen.de)

Published by Copernicus Publications on behalf of the European Geosciences Union.

ACPD
14, 1–49, 2014

Abstract

Mg and Mg^+ concentration fields in the upper mesosphere/lower thermosphere (UMLT) region are retrieved from SCIAMACHY/Envisat limb measurements of Mg and Mg^+ dayglow emissions using a 2-D tomographic retrieval approach. The time series of monthly means of Mg and Mg^+ for number density as well as vertical column density in different latitudinal regions are shown. Data from the limb mesosphere-thermosphere mode of SCIAMACHY/Envisat are used, which covers the 50 km to 150 km altitude region with a vertical sampling of 3.3 km and a highest latitude of 82°. The high latitudes are not covered in the winter months, because there is no dayglow emission during polar night. The measurements were performed every 14 days from mid-2008 until April 2012. Mg profiles show a peak at around 90 km altitude with a density between 750 cm^{-3} and 2000 cm^{-3}. Mg does not show strong seasonal variation at mid-latitudes. The Mg^+ peak occurs 5–15 km above the neutral Mg peak at 95–105 km. Furthermore, the ions show a significant seasonal cycle with a summer maximum in both hemispheres at mid- and high-latitudes. The strongest seasonal variations of the ions are observed at mid-latitudes between 20–40° and densities at the peak altitude range from 500 cm^{-3} to 6000 cm^{-3}. The peak altitude of the ions shows a latitudinal dependence with a maximum at mid-latitudes that is up to 10 km higher than the peak altitude at the equator.

The SCIAMACHY measurements are compared to other measurements and WACCM model results. In contrast to the SCIAMACHY results, the WACCM results show a strong seasonal variability for Mg with a winter maximum, which is not observable by SCIAMACHY, and globally higher peak densities. Although the peak densities do not agree the vertical column densities agree, since SCIAMACHY results show a wider vertical profile. The agreement of SCIAMACHY and WACCM results is much better for Mg^+, showing the same seasonality and similar peak densities. However, there are the following minor differences: there is no latitudinal dependence of the

ACPD
14, 1–49, 2014

peak altitude for WACCM and the density maximum, passing the equatorial region during equinox conditions, is not reduced as for SCIAMACHY.

1 Introduction

The amount of meteoric mass deposited on the earth upper atmosphere every day is estimated to range from 2 to 300 tons. (see, e.g. Table 1 of Plane, 2012, and references therein).

Since the number of extraterrestrial particles encountering the Earth's atmosphere is approximately inversely proportional, in a log-log scale, to the particle's size, the bulk of the daily meteoric mass flux is contributed mainly by particles in the 1–100 micrometer (in radius) size range (Ceplecha et al., 1998; Flynn, 2002; Mathews et al., 2001; Nesvorný et al., 2010, 2011a, b). Furthermore, most of the daily mass input originates from the sporadic meteor background, which is the interplanetary dust forming the Zodiacal dust cloud and which orbits are so evolved that they cannot be traced back to their original parent body (Brown and Jones, 1995; Janches et al., 2006; Fentzke and Janches, 2008). The constant bombardment of particles from the sporadic background contributes far more input that meteor showers (e.g. Murad and Williams, 2002), the latter being a time limited (days to several weeks) enhancement of particles entering the atmosphere in parallel trajectories appearing to radiate from one point in the sky (Jenniskens, 2006). When meteoroids enter the atmosphere at geocentric speeds between 11 to 72 $\mathrm{km\,s^{-1}}$ they collide with air molecules, leading to frictional heating and deceleration. The meteoroids, consisting partly of metals, melt on their surfaces and metals are ablated. The ablation process depends on several factors, like the velocity and entry angle of the meteoroid, the boiling point of the different particles constituents and the size of the meteoroid (see, e.g. McNeil et al., 1998 and Vondrak et al., 2008 for more details). For the micronsize particles of interest to this work, the ablation process occurs between 80 and 125 km. (Vondrak et al., 2008; Janches et al., 2009; Marsh et al., 2013a; Feng et al., 2013) resulting in the deposition of metallic atoms such as

ACPD
14, 1–49, 2014

Sodium, Iron, Potassium and Magnesium in the Mesosphere and Lower Thermosphere (MLT). The observation technique used in this study measures the density of the metal atom and ion layers present in the MLT that are formed with the ablated material from the meteoroids. Once ablated the meteoric metals undergo several chemical reactions (see e.g. Plane, 2003). A fraction of the ablated metals in the ablation region (80 to 105 km) are already in the ionized form. For the case of Mg^+ this fraction is estimated to be negligibly small (Vondrak et al., 2008, Fig. 14.). Mg^+ is formed by charge exchange with the main ion constituents at this altitude NO^+ and O_2^+. The dominant loss process for Mg is the reaction with O_3, which leads to stable oxides, hydroxides and carbonates as reservoir species. Mg^+ is lost by reactions with O_3 but also by reactions with N_2 and other trace gases (CO_2, H_2O) (see, e.g. Fig. 9 in Plane and Whalley, 2012 for a schematic diagram of the most important reactions). The metal molecules condense and form meteoric smoke particles (e.g. Hunten et al., 1980; Kalashnikova et al., 2000; Saunders and Plane, 2006). These meteoric smoke particles can act as condensation nuclei. Heterogeneous condensation of clouds plays an important role in the formation of polar mesospheric clouds in the polar summer mesopause region and also in the formation of polar stratospheric clouds (PSCs) in the polar winter stratosphere. PSCs have an important role in the ozone chemistry and the formation of the ozone hole. In a dynamical equilibrium of meteoroid input and the above mentioned loss reactions, the neutral Mg layer is formed between 85 and 90 km altitude and the Mg^+ layer is formed slightly above the Mg layer (see, e.g. Plane and Helmer, 1995; McNeil et al., 1998 and Plane and Whalley, 2012).

The MLT is not readily probed by in-situ instrumentation, as balloons fly too low, and satellites have to fly higher because of the atmospheric drag that reduces the satellite's operation time. As a result, only rockets carrying in situ instrumentation are able to access this region. These are, however, expensive and rare. Fortunately metal atoms and ions have very strong absorption coefficients and oscillator strengths (see, e.g. Kramida et al., 2012). As a result, although their densities even in the peak region are only a few thousand particles per cubic centimeter, they are very strong emitters of resonance

ACPD
14, 1–49, 2014

fluorescence. Mg and Mg^+ spectral lines are observed at wavelengths below 290 nm. This wavelengths region is strongly affected by ozone absorption in the stratosphere, so that observations from ground are not possible. For this reason the knowledge of the Mg and Mg^+ content in the MLT is poor. In this study the dayglow emission of Mg and Mg^+, detected by the satellite experiment SCIAMACHY (Scanning Imaging Absorption Spectrometer for Atmospheric CHartographY) on Envisat (Environmental Satellite) are used. The Mg and Mg^+ densities are retrieved by the mathematical inversion of these measurements using a radiative transfer model. Mg and Mg^+ have already been obtained from SCIAMACHY by Scharringhausen (2007) and based upon the results of this a new measurements mode for the purpose of better covering the peak region of Mg and Mg^+ has been established and used for this study.

In the study these experimental data are compared to other Mg and Mg^+ measurements as well as simulations of the MLT using a combination of a Meteor Input Function model coupled to a meteor differential ablation model which provides the metal input in the MLT. The result of these models is then used as input in the Whole Atmosphere Climate Community Model (WACCM) with a new chemistry model of Mg and Mg^+ (Plane and Whalley, 2012). WACCM is a general circulation model that incorporates interactive chemistry for both neutral and ion species.

In Sect. 2 a short overview about the SCIAMACHY/Envisat satellite observations and the Mg and Mg^+ density retrieval is provided. In Sects. 3 and 4 the results for Mg and Mg^+ are presented and discussed. In Sect. 5 these findings are compared to other measurements. In Sect. 6 the WACCM-Mg model simulations of Mg and Mg^+ are introduced and the SCIAMACHY dataset is compared to the model results. Finally Sect. 7 summarizes the results obtained in this study.

2 Instrument and algorithm

SCIAMACHY, a satellite-borne grating spectrometer, was launched by ESA (European Space Agency) on Envisat on the 28 February 2002 (see, e.g. Burrows et al., 1995;

ACPD
14, 1–49, 2014

Bovensmann et al., 1999). Envisat flies in a sun-synchronous orbit with a descending node (equatorial crossing time from north to south) at 10:00 a.m. The duration of one orbit is roughly 100 min (15 orbits per day). Note that the local time of SCIAMACHY limb observations changes with latitude. It is ≈ 11 a.m. at 60° N and 9 a.m. at 60° S and, as shown in Fig. 1, varies strongly in the vicinity of the poles. The highest latitude covered by SCIAMACHY limb observations of scattered light is 82°.

Data from SCIAMACHY's limb mesosphere and lower thermosphere (MLT) mode with tangent altitudes between 50 and 150 km in 30 consecutive 3.3 km steps are used in this study. Depending on latitude, consecutive limb measurements have a latitudinal separation of up to 8°, because nadir measurements are performed between two MLT-measurements. However, there is a small latitude offset between MLT measurements in two consecutive orbits. MLT-measurements were performed from mid 2008 until the loss of contact to Envisat in April 2012. MLT-measurements were performed roughly every two weeks for 15 consecutive orbits, which corresponds to one day of consecutive measurements. Apart from a few days, where some orbits are missing in the data, all longitudes are equally covered (sampling every 24° of longitude). The two dimensional retrieval algorithm uses all measurements of one orbit and retrieves the metal densities from each emission line of the species on a latitude and altitude grid. For averaged data, a reference orbit for geolocations is used, which is formed from the dataset to average. Measurements with similar latitudes and local times as the measurements of the reference orbit are averaged. A comprehensive discussion of the algorithm and error estimation was made by Langowski et al. (2013). For Mg the spectral line at 285.2 nm is used. For Mg^+ the spectral lines at 279.6 nm and 280.4 nm are used.

It has to be noted that the first measurements at the start of each orbit are contaminated by solar stray light, which can be seen in the dark signal measurement at 350 km tangent altitude. These measurements, as well as the next consecutive measurements, which do not show solar stray light in the dark signal, have been sorted out for this study. The strong solar stray light contaminated measurements actually

ACPD
14, 1–49, 2014

show reasonable profiles. However, the measurement in between the stray light and not stray light contaminated measurements showed strongly different features than the neighboring measurements. At some days similar features for the remaining highest northern latitude measurements (after excluding the stray light measurements) still can be seen. This features are not dependent of the orbit phase anymore, but only appear at latitudes > 78° N. The actual grid for calculating the densities has a larger extend and the outermost latitude intervals have been cut off to reduce edge effects, which may, however, affect the neighboring latitudes.

3 Seasonal variations of Mg

The seasonal variations in altitude and latitude of Mg and Mg^+ are investigated in this study. Prior to averaging, measurements at night or those having noise peaks in the investigated spectral region, caused by highly energetic particles hitting the detector (e.g. in the Southern Atlantic Anomaly region), are filtered from the data set. The limb spectra of up to 15 daily single orbits are zonally averaged before running the retrieval algorithm, in order to improve the signal to noise ratio. To further reduce the noise in the results, all January results, February results, etc. are averaged for the entire measurement period.

The algorithm retrieves densities on an altitude and latitude grid with 40 equidistant day side latitude intervals between 82° S and N and 80 altitude intervals with 1 km thickness between 70 and 150 km, additionally there are night side latitude intervals to overcome ambiguities of identical latitudes but different local time at high-latitudes. The monthly averaged results for Mg are shown in Fig. 2.

Mg shows a peak at around 90 km with densities up to 1750 cm^{-3}. There is a strong month-to-month variability in the latitudinal distribution. The averaged yearly results are shown in Fig. 3. In the yearly average, the densities in the low latitudes are higher than at the high latitudes in the peak region. At the highest covered southern latitude there

ACPD
14, 1–49, 2014

are increased densities above 100 km, which, however, are most likely caused by the fact that this latitude is less covered and therefore has a larger statistical error.

Figure 4 shows the seasonal variation of the vertical profile for low-, mid- and high-latitudes, and Fig. 5 shows the vertical column densities (VCDs). The month-to-month variations are large, and thus the error on the estimate of the amplitude of seasonal variations for mid-latitudes is relatively large. The seasonal variation of the Mg peak altitude is estimated to be less than 5 km.

The VCD varies between 0.5×10^9 cm^{-2} and 3.5×10^9 cm^{-2}. The VCD between 40° N and 40° S is higher than for higher latitudes, which are only covered in the hemispheric summer. The seasonal variation is small compared to the mean of the vertical column densities. This relatively small variation is required to retrieve the correct mean value (because of non-linearities in the retrieval) as comprehensively discussed by Langowski et al. (2013).

4 Seasonal variations of Mg^+

For Mg^+ the same approach for data averaging is used, as described for Mg in Sect. 3. For Mg^+ there are two spectral lines, one at 279.6 nm and the second one at 280.4 nm. Mg^+ densities are independently retrieved from both lines. The differences in the peak region are lower than 25 %. The densities on an altitude and latitude grid for the monthly averaged results are shown in Figs. 6 and 7.

The Mg^+ densities peak at an altitude of 95–105 km with peak densities of 500–6000 cm^{-3}. The peak densities show a seasonal variation with a summer maximum between 25–45° in both hemispheres. In summer the highest peak altitude is roughly at 45° (N and S). It occurs around 105 km, which is up to 10 km higher than the lowest peak altitude at the equator and higher than that at the poles. There is a minimum at the equator and also a second maximum in peak altitude in the mid-latitudes on the winter hemisphere, that, however, is more variable than the one in the summer hemisphere.

ACPD
14, 1–49, 2014

The latitudinal variation of Mg^+ is also seen in the average over all available measurements in 2008–2012, which is shown for both lines in Fig. 8. The latitudinal dependence of the peak altitude seems to be symmetric towards the equator. However, there is an asymmetry in the peak density, which is close to two times as big for the Northern Hemisphere than for the Southern Hemisphere. When looking at the densities above the maximum density region for mid and low latitudes the density at same altitude is lower in the equatorial region than at 40° below 110 km, while this behavior is reversed above ≈ 110 km. Furthermore, the density at the uppermost altitude level is enhanced in the equatorial region, pointing to the abundance of Mg^+ above this altitude. This may be explained by enhanced vertical upward transport in the equatorial region.

The equatorial electron distribution with transport from the equator to higher latitudes has been observed in ionospheric soundings. It is known as the equatorial anomaly or Appleton anomaly (Kendall and Windle, 1965). Typically there are fewer electrons at the equator than at 20° on either side of the equator due to this transport. In situ satellite measurements of the metals above 120 km have been carried out using the Atmospheric Explorer satellite. A discussion of these data can be found in Grebowsky and Aikin (2002). The vertical upward transport of Mg^+ ions near the equator has been discussed, e.g. in Hanson and Sterling (1972). The sun is passing the equatorial region from east to west. The ionisation in the thermosphere is strong for low solar zenith angles (SZAs) which leads to denser plasmas there. The heavier ions and the lighter electrons gyrate in different directions in the Earth's magnetic field pointing from north to south at the equator. This leads to a charge separation, which produces an eastwards pointed electric field and a westward current of the electrons. The magnetic field along the meridians and the electric field along the equator lead to an $E \times B$-Drift perpendicular to both in the radial direction, resulting in a strong upward polarization field. This polarization field accelerates the ions to higher altitudes and even above the F-layer. However, this effect can only explain an upward transport within ±3° latitude. Fesen et al. (1983) showed that additionally neutral meridional winds have to be taken into account in order to explain vertical transport also at higher latitudes up to 30°

ACPD
14, 1–49, 2014

and this was experimentally shown, e.g. in Fesen and Hays (1982a, b); Gérard and Monfils (1978). As for Mg the annual means show higher densities above 110 km at the northernmost and southernmost latitudes due to less coverage and therefore higher statistical errors. However, at high northern latitudes, which are cut off in the shown results, high densities can be retrieved when also using the stray light contaminated measurements. This is shown in Fig. 9. The results as well as the input raw data show low densities below 90 km and at different altitudes in between the high signal region, which makes a differentiation between a stray light effect and a true metal emission complicated. Should this feature be real it could be explained by the cleft ion fountain found by Lockwood et al., 1985, which describes the transport of charged particles along the magnetic field lines, which close at the pole. This transport may lift charged particles up to several earth radii until they become neutralized and sink down if they are heavy enough and are not quickly ionized again.

Figures 10 and 11 show the seasonal variation of the vertical Mg^+ profile for low-, mid- and high-latitudes for both Mg^+ emission lines, and Fig. 12 shows the VCDs for both lines. In each of the latitude regions, a maximum in peak altitude is found for the summer time in the corresponding hemisphere.

The VCD varies between $1 \times 10^9\,cm^{-2}$ and $11 \times 10^9\,cm^{-2}$. A seasonal cycle with a summer maximum is observed and the strongest variations are observed between 20° and 40°. Figure 13 shows the ratio of Mg^+ and Mg VCDs. For low- and mid- latitudes as well as the high latitudes in the southern hemispheric summer the ratio is in between 0.5 and 4. The seasonal variability of the ratio follows the one of Mg^+, as Mg does not show a strong seasonal variability.

5 Comparison to other measurements

Mg and Mg^+ cannot be observed from the ground, because the wavelengths of the lines are below 300 nm and the emission signal is absorbed strongly by ozone in the stratosphere. As a result, only few measurements are available and rely on observations from

ACPD
14, 1–49, 2014

sounding rockets and satellites. The first rocket-borne ion mass spectrometer measurement of metal ions was performed by Johnson and Meadows (1955) (May 1954, White Sands) and enhanced ion signals between 93 and 124 km were found. According to Grebowsky and Aikin (2002) approximately 50 flights of rocket-borne mass spectrometers, probing the region between 80 and 130 km have been performed since then (until 2002). Other density profiles for Mg^+ can be found in Istomin (1963); Narcisi and Bailey (1965); Narcisi (1971); Aikin and Goldberg (1973); Philbrick et al. (1973); Zbinden et al. (1975); Herrmann et al. (1978); Kopp and Herrmann (1984); Kopp et al. (1985b, a); Kopp (1997); Roddy et al. (2004). Date, local time, latitude and reference publications of these and other rocket flights can also be found in Table 1 of Grebowsky et al. (1998).

A disadvantage for the comparison with the new dataset presented is that most of these measurements were performed during special events with E_s layers, aurora, meteor showers, stratospheric warmings or noctilucent clouds present. Often sporadic Mg^+ layers occured between 105–110 km and/or 120 km. The Mg^+ peak altitude in most of these measurements can be found between 90 and 95 km altitude and the full width at half maximum (FWHM) of the layers is on the order of 5–10 km, but sometimes the FWHM is only 1 km.

When comparing in-situ mass spectrometer measurements with satellite remote sensing results, it has to be remembered that the in-situ measurements are much more localized and limited to the direct vicinity of the rocket. In contrast, remote sensing techniques typically cover a large volume with horizontal distances along and perpendicular to the viewing direction of several hundreds of kilometers. This results in smoother layers with a larger FWHM for the remote sensing method. The width of the Mg^+ layers as well as the peak densities presented in this study are in good agreement with the in-situ rocket measurements. However, the strong latitudinal dependence of the peak altitude observed in Figs. 10 and 11 is not found in the in-situ rocket data. In addition to the in-situ measurements with rockets, there are also airglow measurements available, from rockets, space shuttles and satellites. However, to retrieve density in-

ACPD
14, 1–49, 2014

formation from this method radiative transfer models as well as inversion techniques and computational power is needed. Therefore, often only slant column information is available (see, e.g. Boksenberg and Gérard, 1973 or Gérard and Monfils, 1974). In Anderson and Barth (1971) (Summer, $\approx 40^{\circ}$ N) the region up to 106 km altitude is scanned during a sporadic E_s layer event, and the peak altitude of the Mg^+ is not reached during this flight, i.e. was higher than 106 km. No Mg signal above the instrumental noise was observed in these spectra. The region above the peak altitude from 150 km up to the F-layer and above is investigated in Gérard and Monfils (1978); Fesen and Hays (1982a); Mende et al. (1985); Gardner et al. (1995, 1999) and typically shows less than $100\,cm^{-3}$ Mg^+ ions at 150 km. This is in good agreement with the profiles described in Sect. 4. In some plots higher densities can be seen in the profiles retrieved from the limb observations of SCIAMACHY. These are explained by retrieval artifacts on the edge of the retrieval grid and vertical constraints tuned for the main peak. These allow small oscillations, compared to the main peak, in regions with lower densities. Since these artifacts appear at the upper edge of the profile it also hints that there is a significant density above the highest tangent altitude for Mg^+. In Minschwaner et al. (2007) a combined NO and Mg^+ retrieval for satellite limb measurements is shown, which is in good agreement with the results in Sect. 4 in terms of the Mg^+ concentrations at peak altitude and at the upper edge of the profile. However, the Mg^+ peak altitude is at 90 km. Taking into account the coarser sampling (every 7 km), higher statistical errors and a tangent height offset (±4 km) in Minschwaner et al. (2007), the agreement is reasonable. Tangent height offset of a similar magnitude was also an issue for SCIAMACHY (von Savigny et al., 2005), however, this error was reduced to (±200 m) (von Savigny et al., 2009). The NO Band emission, which overlaps with the Mg^+ lines and the Mg line, is on the same order of magnitude as the Mg^+ lines in Minschwaner et al. (2007) and even bigger than the Mg emission, which made a NO correction necessary. The SCIAMACHY MLT dataset does not show these strong NO lines at 280 and 285 nm. NO in this region is very sensitive to solar activity. Results for NO retrievals from the same SCIAMACHY dataset used in this study are reported by Bender et al.

ACPD
14, 1–49, 2014

(2013). These exhibit densities of the same order of magnitude as the equatorial density plot for NO in Minschwaner et al. (2007), only at high-latitudes in summer and winter and from late 2011 to 2012. However, we did not observe clear NO signals in the vicinity of the Mg/Mg^+ lines in this period. A time series of Mg^+ vertical columns covering several years and retrieved from SBUV nadir measurements was presented by Joiner and Aikin (1996). These measurements were performed approximately 1 day per month, with a spectral resolution of 1.13 nm and a spectral sampling every 0.2 nm (a factor 5 for the resolution, and 2 for the sampling, worse than SCIAMACHY). The results in Joiner and Aikin (1996) are in very good agreement with the results obtained in this study, especially when comparing Figs. 10 and 11 in Joiner and Aikin (1996) with Fig. 12 in this study. Mg was also investigated in Joiner and Aikin (1996). However, the average VCD for the rare profiles, where the signal was significant, is 4×10^{10} cm^{-2}, which is a factor 10 more than the VCDs in Fig. 5.

Satellite measurements with long time series and daily coverage are available from GOME and GOME-2 in nadir mode and from SCIAMACHY in nadir and nominal limb mode. All 3 instruments have a similar spectral resolution. The GOME dataset was investigated for Mg^+ and Mg VCDs in Correira et al. (2008, 2010) and Correira (2009). Figures 1 and 2 in Correira et al. (2008) show Mg and Mg^+ VCDs for 1996 and 1997 as well as the Mg^+ to Mg ratio for latitude intervals from 0–10° and 30–40° for both hemispheres. For the low-latitudes, where there is less seasonality the VCDs for Mg^+ are at $6–7 \times 10^9$ cm^{-2} which is higher than in Fig. 12, the Mg densities are at 3×10^9 cm^{-2} which is a similar magnitude to that in Fig. 5. In the equatorial region the Mg columns agree better, and a higher VCD in the Nadir results for Mg^+ can be explained by the thermospheric part of Mg^+ which is not part of the VCDs in Fig. 12. At mid-latitudes Mg^+ shows a strong seasonal cycle with a summer maximum in Correira et al. (2008). This seasonality is quite symmetric for both hemispheres and the bigger VCDs can be found in the Southern Hemisphere. Furthermore, the summer maximum at mid latitudes does not exceed the VCDs at low-latitudes. For Mg a summer maximum is ob-

ACPD
14, 1–49, 2014

served which is more pronounced in the Southern Hemisphere. The Mg^+ to Mg VCD ratios in Correira et al. (2008) are in good agreement with our results shown in Fig. 13.

The nominal limb mode dataset, covering the tangent height range from the surface up to 92 or 105 km (only until early 2003), respectively, combined with the nadir mode dataset from SCIAMACHY from 2002 to 2007 was investigated in Scharringhausen et al. (2008b, a) and Scharringhausen (2007). The peak region for the ions could not be fully resolved with the nominal limb mode, however, the agreement for ions is quite good showing only slightly higher VCD in Scharringhausen (2007) compared to the results in this study. In the Southern Hemisphere the seasonal cycle was not identified well in Scharringhausen (2007), which agrees with the results presented in Fig. 12 showing a weaker seasonal cycle in this region. At the very beginning of the Scharringhausen VCD dataset in 2002 (e.g. Figs. 69 and 70 in Scharringhausen, 2007) slightly higher VCDs for both species are observed than for the other years. This may come from increased NO signals near the Mg/Mg^+ lines during solar maximum. Another reason for the higher Mg^+ VCDs in 2002 may also be the change of the maximum tangent altitude from 105 to 95 km. More differences to Scharringhausen (2007) can be found in the Mg data, since the Mg line is much more affected by newly added radiative transfer features. There was no correction of the Ring effect in Scharringhausen (2007), which led to high densities below 80 km and a density maximum at the lower edge of the retrieval boundaries at 70 km. This inelastic scattering contribution additionally adds a seasonal variation to the dataset. Furthermore, the Mg line at 285.2 nm is much more affected by self absorption of the emission, which was not considered in Scharringhausen (2007), so the Mg VCDs were smaller than reported here. However, most of the findings from the further analysis of the Scharringhausen dataset are only weakly affected by these differences and are still valid.

In summary it can be concluded, that the Mg/Mg^+ results presented here are in good agreement with previous satellite and rocket instruments. The most striking difference to previous measurements is the strong latitudinal dependence of the peak altitude of Mg^+ with differences of up to 10 km for different latitudinal zones.

ACPD
14, 1–49, 2014

6 Comparison of Mg and Mg^+ observed by SCIAMACHY and modelled by the WACCM model

6.1 WACCM Model

WACCM is a high-top chemical-dynamical model, which simulates the altitudes from the earth's surface up to 140 km (Garcia et al., 2007; Marsh et al., 2007, 2013b). Here we use the specified dynamics SD-WACCM, which is nudged by the GEOS5 meteorological dataset (including temperature, specific humidity, horizontal winds) below 60 km. This is the same version used by Feng et al. (2013) and Marsh et al. (2013a) who successfully incorporated iron and sodium chemistry into WACCM. Here we develop a global model of meteoric magnesium in the atmosphere by combining three components: a treatment of the injection of meteoric constituents into the atmosphere (Feng et al., 2013; Marsh et al., 2013a), a description of the neutral and ion-molecule chemistry of magnesium in the mesosphere and lower thermosphere (Whalley and Plane, 2010; Plane and Whalley, 2012) and WACCM. The Mg meteoroid injection function (MIF) has a similar seasonal variability as those of Fe and Na. The minimum MIF is in the spring with an ablation flux of 1300 atoms $cm^{-2}\,s^{-1}$, and the maximum occurs in the autumn with 2400 $cm^{-2}\,s^{-1}$. The peak ablation height is around 95 km. These fluxes are obtained by scaling the Mg MIF to match the observed Mg column density. This requires dividing the Mg ablation flux by a factor of 15, relative to that of Na (Marsh et al., 2013a). Since the relative chondritic abundance of Mg is 16 times that of Na, this means that the ablation fluxes of Mg and Na are similar in the model. Tables 1–3 list the Mg chemical reactions and their rate coefficients added to the standard chemistry scheme in this study.

An important magnesium reservoir on the underside of the Mg layer is $Mg(OH)_2$. This is reduced back to Mg via MgOH by reaction with H atoms (R12). The subsequent reaction with H atoms (R12b) is most likely faster than R12, and so the reaction rate is not explicitly in Table 2 (Plane and Whalley, 2012). The polymerization of MgO_2H_2 to form meteoric smoke is parameterised by a dimerization rate coefficient (reaction

ACPD
14, 1–49, 2014

R13 in Table 2). This reaction should be essentially at the high pressure limit even in the upper mesosphere because of the large number of atoms in the dimer and the large binding energy (268 kJ mol^{-1}, calculated at the B3LYP/6-311+g(2d, p) level of electronic structure theory (see, e.g. Frisch et al., 2009). The capture rate coefficient is then increased to 9×10^{-10} cm^3 molecule^{-1} s^{-1} to account for the concentration of other metallic species (e.g. $NaHCO_3$, FeOH etc) with which MgO_2H_2 can also polymerize.

The model was run for the period 2004 to 2011, when the GEOS5 analysis data are available. To derive the modeled climatologies of temperature, Mg and other chemical constituents, we use the model output from 2005 to 2011.

6.2 Comparison of WACCM model and SCIAMACHY measurements results

Figure 14 shows the monthly mean results for 7 yr of WACCM simulations of Mg from 2005 to 2011 and Fig. 15 shows the same for Mg^+. Figure 16 shows the VCDs for both Mg and Mg^+. Mg shows a clear seasonal cycle with a winter maximum which is most pronounced at the poles. The peak altitude is nearly constant, but small seasonal variations can be found. E.g. in February the peak altitude at the poles is roughly 85 km, while it is [5] km higher at 90 km in the equatorial region. Mg^+ shows a seasonal cycle with a summer maximum. In addition, there is an increased Mg^+ density at the poles, even in the winter hemisphere. The Mg^+ peak altitude is close to 95 km and shows no strong variation, with latitude and time. The seasonal variations in the VCD profiles for Mg and Mg^+ are very similar to Na and Na^+ profiles (Fig. 3 in Marsh et al., 2013a). In contrast to the SCIAMACHY measurements, which are made at one particular local time, daily averaged output is used for WACCM. We also colocated the WACCM dataset to SCIAMACHY local time and latitudinal coverage, but found only small differences to the non collocated daily average mean of WACCM. There is a diurnal variation of the vertical column density in the WACCM data, but nearly no diurnal variation for the the vertical profile shape. Figures 17 and 18 show the direct comparison of SCIAMACHY and WACCM annual means for Mg and Mg^+. We used the colocated data for both plots, since these are the only plots with significant differences between uncollo-

ACPD
14, 1–49, 2014

cated daily means and colocated data, for latitudes higher than 40°. Figures 19 and 20 show the comparison for the vertical profile only.

In the annual mean profile the peak density of Mg for WACCM is higher than for SCIAMACHY. However, the peak width of the SCIAMACHY profile is wider than for WACCM and the VCDs are very similar, which is expected, because the Mg MIF is scaled (see above). The peak altitude of WACCM (88 km) and SCIAMACHY (90 km) results agree very well considering the 3.3 km step size in the SCIAMACHY measurements and the vertical sampling step size of 2 km for WACCM and 1 km for SCIAMACHY. One explanation for the wider SCIAMACHY peak is a strong Ring effect influence (Grainger and Ring, 1962) for the Mg spectral line, which has not adequately been corrected. At the lower and upper peak edge, the SCIAMACHY number densities are not zero. This may be related to the requirement in the retrievals that the densities must be positive, which is needed for stability in the retrieval. However, the densities are smaller than the single day error there. The agreement of WACCM and SCIAMACHY is better for Mg^+. The WACCM Mg^+ peak and column densities are of similar magnitude as the SCIAMACHY results and also show the same seasonal variability with a summer maximum. There are also small differences: the maximum in the WACCM data is not reduced when passing the equatorial region during equinox and also has a stronger extension to the higher latitudes in summer. Furthermore, a second maximum appears in the winter hemisphere at high-latitudes, which is not covered by SCIAMACHY measurements and so is not observed. The WACCM results also do not show the strong seasonality and latitude dependence of the peak altitude, that can be found in the SCIAMACHY results. The peak altitude at 95 km is in slightly better agreement with the rocket data than with SCIAMACHY. One reason for some of these discrepancies between model and observations is that WACCM does not include the Lorentz $\boldsymbol{v} \times \boldsymbol{B}$-force, as discussed in Feng et al. (2013). In a global average of the profile, however, the differences are small. The lower peak edge of Mg^+ is in better agreement than for Mg, since, e.g. the Ring effect influence is much weaker for Mg^+ than for Mg.

ACPD
14, 1–49, 2014

The agreement of the peak edge becomes worse with larger distance from the peak altitude. Nevertheless, the FWHM of the peak is in good agreement.

7 Summary and conclusions

Monthly averaged global vertical and latitudinal density distributions of Mg and Mg^+ retrieved from the SCIAMACHY limb MLT measurements from 2008 to 2012 have been shown. The MLT measurements cover the vertical region between 70 km and 150 km and have a good resolution in the peak region. Mg shows highly variable results and variabilities are mostly affected by the measurements error and no clear seasonal cycle can be observed for Mg. The peak altitude of Mg is nearly constant at ≈ 90 km for all latitudes and times. Mg^+ shows a clear seasonal cycle with a summer maximum in the peak density, most pronounced at mid-latitudes. Furthermore, Mg^+ shows a seasonal variation of the peak altitude, with higher altitudes in the summer, as well as a latitudinal dependence of the peak altitudes with up to 5–10 km higher altitudes at mid-latitudes compared to the equatorial peak altitude at 95 km.

The SCIAMACHY results are reasonably consistent with previously published rocket profiles. There is a good agreement for the peak density values as well as the seasonality for Mg^+. However, the rocket measurements do not show the latitudinal dependence of the peak altitude, but typically show peak altitudes at slightly below 95 km.

The SCIAMACHY results were compared with WACCM model results. There is a disagreement in the seasonal variation for Mg between SCIAMACHY and WACCM results, with WACCM showing a clear seasonal cycle with a winter maximum at the poles. Furthermore, the WACCM peak densities are roughly a factor 2 bigger than the SCIAMACHY peak densities. The peak altitude and peak shape are in good agreement with SCIAMACHY, showing a slightly wider profile. The combination of higher peak densities for WACCM, but wider peak profile for SCIAMACHY leads to very similar values for the VCDs. The agreement between WACCM and SCIAMACHY is better for Mg^+ than for Mg. Both SCIAMACHY and WACCM show a clear seasonal cycle with a sum-

ACPD
14, 1–49, 2014

mer maximum and the peak densities are in good agreement. However, like the rocket measurements, WACCM does not show a latitudinal dependence of the peak altitude. The peak shape of Mg^+ agrees very well for WACCM and SCIAMACHY in the high density region, where the SCIAMACHY error is low.

Acknowledgements. We wish to thank the AFOSR and the EOARD for the financial support of the project granted by grant#FA8655-09-3012.

SCIAMACHY is jointly funded by Germany, the Netherlands and Belgium. This work was in part supported by the University of Bremen and Ernst-Moritz-Arndt-University of Greifswald. SCIAMACHY data was kindly provided by the European Space Agency (ESA). The WACCM-Mg modelling work was supported by the UK Natural Environment Research Council (NERC grant NE/G019487/1). The National Center for Atmospheric Research is operated by the University Corporation for Atmospheric Research under sponsorship of the National Science Foundation.

References

Aikin, A. C. and Goldberg, R. A.: Metallic ions in the equatorial ionosphere, J. Geophys. Res., 78, 734–745, 1973. 12

Anderson, J. G. and Barth, C. A.: Rocket investigation of the Mg I and Mg II dayglow, J. Geophys. Res., 76, 3723–3732, 1971. 13, 29

Bender, S., Sinnhuber, M., Burrows, J. P., Langowski, M., Funke, B., and López-Puertas, M.: Retrieval of nitric oxide in the mesosphere and lower thermosphere from SCIAMACHY limb spectra, Atmos. Meas. Tech., 6, 2521–2531, doi:10.5194/amt-6-2521-2013, 2013. 13

Boksenberg, A. and Gérard, J. C.: Ultraviolet observations of equatorial dayglow above the F_2 Peak, J. Geophys. Rev., 78, 4641–4650, 1973. 13

Bovensmann, H., Burrows, J. P., Buchwitz, M., Frerick, J., Noël, S., Rozanov, V. V., Chance, K. V., and Goede, A. P. H.: SCIAMACHY: mission objectives and measurement modes, J. Atmos. Sci., 56, 127–150, 1999. 7

Brown, P. and Jones, J.: A determination of the strengths of the sporadic radio-meteor sources, Earth Moon Planets, 68, 223–245, 1995. 4

ACPD
14, 1–49, 2014

Burrows, J. P., Hölzle, E., Goede, A. P. H., Visser, H., and Fricke, W.: SCIAMACHY–scanning imaging absorption spectrometer for atmospheric chartography, Acta Astronaut., 35, 445–451, 1995. 6

Ceplecha, Z., Borovička, J., Elford, W. G., Revelle, D. O., Hawkes, R. L., Porubčan, V., and Šimek, M.: Meteor phenomena and bodies, Space Sci. Rev., 84, 327–471, 1998. 4

Correira, J.: Temporal and Spatial Distribution of Metallic Species in the Upper Atmosphere, Ph.D. thesis, 2009TS1. 14

Correira, J., Aikin, A. C., Grebowsky, J. M., Pesnell, W. D., and Burrows, J. P.: Seasonal variations of magnesium atoms in the mesosphere-thermosphere, Geophys. Res. Lett., 35, 330–337, 2008. 14, 15, 42

Correira, J., Aikin, A. C., Grebowsky, J. M., and Burrows, J. P.: Metal concentrations in the upper atmosphere during meteor showers, Atmos. Chem. Phys., 10, 909–917, doi:10.5194/acp-10-909-2010, 2010. 14

Feng, W., Marsh, D. R., Chipperfield, M. P., Janches, D., Hoffner, J., Yi, F., and Plane, J. M. C.: A global atmospheric model of meteoric iron, J. Geophys. Res.-Atmos., 118, 9456–9474, 2013. 4, 16, 18

Fentzke, J. T. and Janches, D.: A semi-empirical model of the contribution from sporadic meteoroid sources on the meteor input function observed at arecibo, J. Geophys. Res., 113, A03304,TS2, 2008. 4

Fesen, C. G., and Hays, P. B.: Mg^+ Morphology from visual airglow experiment observations, J. Geophys. Res., 87, 9217–9223, 1982a. 11, 13

Fesen, C. G., and Hays, P. B.: Two-dimensional inversion technique for satellite airglow data, Appl. Optics, 21, 3784–3791, 1982b. 11

Fesen, C. G., Hays, P. B., and Anderson, D. N.: Theoretical Modelling of Low-Latitude Mg^+, J. Geophys. Res., 88, 3211–3223, 1983. 10

Flynn, G.: Chapter 4 in: Meteors in the Earth's Atmosphere, edited by: Murad, E. and Williams, I. P., Cambridge University Press, Cambridge, 2002. 4

Frisch, M., Trucks, G., Schlegel, H., Scuseria, G., Robb, M., Cheeseman, J., Scalmani, G., Barone, V., Mennucci, B., Petersson, G., Nakatsuji, H., Caricato, M., Li, X., Hratchian, H., Izmaylov, A., Bloino, J., Zheng, G., Sonnenberg, J., Hada, M., Ehara, M., Toyota, K., Fukuda, R., Hasegawa, J., Ishida, M., Nakajima, T., Honda, Y., Kitao, O., Nakai, H., Vreven, T., J. A. Montgomery, J., Peralta, J., Ogliaro, F., Bearpark, M., Heyd, J., Brothers, E., Kudin, K., Staroverov, V., Kobayashi, R., Normand, J., Raghavachari, K., Rendell, A.,

Please note the remarks at the end of the manuscript.

ACPD
14, 1–49, 2014

Global investigation of the Mg atom and ion layers

M. Langowski et al.

Burant, J., Iyengar, S., Tomasi, J., Cossi, M., Rega, N., Millam, J., Klene, M., Knox, J., Cross, J., Bakken, V., Adamo, C., Jaramillo, J., Gomperts, R., Stratmann, R., Yazyev, O., Austin, A., Cammi, R., Pomelli, C., Ochterski, J., Martin, R., Morokuma, K., Zakrzewski, V., Voth, G., Salvador, P., Dannenberg, J., Dapprich, S., Daniels, A., Farkas, O., Foresman, J., Ortiz, J., Cioslowski, J., and Fox, D.: Gaussian 09, Revision A.1, Gaussian Inc, available at: www.gaussian.comTS3, 2009. 17

Garcia, R. R., Marsh, D. R., Kinnison, D. E., Boville, B. A., and Sassi, F.: Simulation of secular trends in the middle atmosphere, 1950–2003, J. Geophys. Res., 112, D09301TS4, 2007. 16

Gardner, J. A., Viereck, R. A., Murad, E., Knecht, J., Pike, C. P., Broadfoot, A. L., and Anderson, E. R.: Simultaneous observations of neutral and ionic magnesium in the thermosphere, Geophys. Res. Lett., 22, 2119–2122, 1995. 13

Gardner, J. A., Broadfoot, A. L., McNeil, W. J., Lai, S. T., and Murad, E.: Analysis and modeling of the GLO-1 observations of meteoric metals in the thermosphere, J. Atmos Sol.-Terr. Phy., 61, 542–562, 1999. 13

Gérard, J. C. and Monfils, A.: Satellite Observations of the Equatorial Mg II Dayglow Intensity Distribution, J. Geophys. Rev., 79, 2544–2550, 1974. 13

Gérard, J. C. and Monfils, A.: The MgII Equatorial Airglow Altitude Distribution, J. Geophys. Res., 83, 4389–4391, 1978. 11, 13

Grainger, J. and Ring, J.: Anomalous Fraunhofer Line Profiles, Nature, 193, 762, 1962. 18

Grebowsky, J. M. and Aikin, A. C.: Chapter 8 in: Meteors in the Earth's Atmosphere, edited by: Murad, E. and Williams, I. P., Cambridge University Press, Cambridge, 2002. 10, 12

Grebowsky, J. M., Goldberg, R. A., and Pesnell, W. D.: Do meteor showers significantly perturb the ionosphere?, J. Atmos. Sol.-Terr. Phy., 60, 607–615, 1998. 12

Hanson, W. B. and Sterling, D. L.: Source and Identification of Heavy Ions in the Equatorial F Layer, J. Geophys. Res., 77, 5530–5541, 1972. 10

Herrmann, U., Eberhardt, P., Hidalgo, M. A., and Kopp, E.: Metal ions and isotopes in sporadic E-layer during Perseid meteor shower, Space Res., 18, 249–252, 1978. 12

Hunten, D. M., Turco, R. P., and Toon, O. B.: Smoke and dust particles of meteoric origin in the mesosphere and stratosphere, J. Atmos. Sci., 37, 1342–1357, 1980. 5

Istomin, V.: Ions of extra-terrestrial origin in the earth's ionosphere, Planet. Space Sci., 11, 173–181, 1963. 12

Please note the remarks at the end of the manuscript.

ACPD
14, 1–49, 2014

Global investigation of the Mg atom and ion layers

M. Langowski et al.

Janches, D., Heinselman, C., Chau, J., Chandran, A., and Woodman, R.: Modeling the global micrometeor input function in the upper atmosphere observed by high power and large aperture radars, J. Geophys. Res., 111, A07317TS5, 2006. 4

Janches, D., Dyrud, L. P., Broadley, S. L., and Plane, J. M. C.: First observations of micrometeoroid differential ablation in the atmosphere, Geophys. Res. Lett., 36, L06101TS6, 2009. 4

Jenniskens, P.: Meteor Showers and Their Parents Comets, Cambridge University Press, Cambridge, 2006. 4

Johnson, C. Y. and Meadows, E. B.: First Investigation of Ambient Positive-Ion Compostion to 219 km by Rocket-Borne Spectrometer, J. Geophys. Res., 60, 193–203, 1955. 12

Joiner, J. and Aikin, A. C.: Temporal and spatial variations in upper atmospheric Mg^+, J. Geophys. Res., 101, 5239–5250, 1996. 14

Kalashnikova, O., Horanyi, M., Thomas, G. E., and Toon, O. B.: Meteoric smoke production in the atmosphere, Geophys. Res. Lett., 27, 3293–3296, 2000. 5

Kendall, P. C. and Windle, D. W.: The Appleton anomaly, Nature, 207, 964–965, 1965. 10

Kopp, E.: On the abundance of metal ions in the lower ionosphere, J. Geophys. Res., 102, 9667–9674, 1997. 12

Kopp, E. and Herrmann, U.: Ion composition in the lower ionosphere, Ann. Geophys.-Italy, 2, 83–94, 1984. 12

Kopp, E., Eberhardt, U., Herrmann, U., and Björn, L.: Positive ion composition of the high latitude summer D-region with noctilucent clouds, J. Geophys. Res., 90, 13041–13053, 1985a. 12

Kopp, E., Ramseyer, H., and Björn, L.: Positive ion composition and electron density in a combined auroral and NLC event, Adv. Space. Res., 4, 157–161, 1985b. 12

Kramida, A., Ralchenko, Y., Reader, J., and NIST ASD Team (2012)TS7: NIST Atomic Spectra Database (version 5.0), 2012.TS8 5

Langowski, M., Sinnhuber, M., Aikin, A. C., von Savigny, C., and Burrows, J. P.: Retrieval algorithm for densities of mesospheric and lower thermospheric metal and ion species from satellite borne limb emission signals, Atmos. Meas. Tech. Discuss., 6, 4445–4509, doi:10.5194/amtd-6-4445-2013, 2013. 7, 9

Lockwood, M., Horwitz, J. R., Chandler, M. O., Waite, J. H., Moore, T. E., and Chappel, C. R.: The cleft ion fountain, J. Geophys. Res., 90, 9736–9748, 1985. 11

Please note the remarks at the end of the manuscript.

ACPD
14, 1–49, 2014

Global investigation of the Mg atom and ion layers

M. Langowski et al.

Marsh, D. R., Garcia, R. R., Kinnison, D. E., Boville, B. A., Sassi, F., Solomon, S. C., and Matthes, K.: Modeling the whole atmosphere response to solar cycle changes in radiative and geomagnetic forcing, J. Geophys. Res., 112,TS9, 2007. 16

Marsh, D. R., Janches, D., Feng, W., and Plane, J. M. C.: A global model of meteoric sodium, J. Geophys. Res.-Atmos., 118, 11442–11452, 2013a. 4, 16, 17

Marsh, D. R., Mills, M. J., Kinnison., D. E., Lamarque, J. F., Calvo, N., and Polvani, L. M.: Climate Change from 1850 to 2005 Simulated in CESM1(WACCM), J. Climate, 26, 2013b. 16

Martinez-Nunez, E., Whalley, C. L., Shalashilin, D., and Plane, J. M. C.: Capture, collisional stabilization and collision-induced dissociation, J. Phys. Chem. A, 114, 6472–6479, 2010. 29

Mathews, J. D., Janches, D., Meisel, D. D., and Zhou, Q.-H.: The micrometeoroid mass flux into the upper atmosphere: Arecibo results and a comparison with prior estimates, Geophys. Res. Lett., 28, 1929–1932, 2001. 4

McNeil, W. J., Lai, S. T., and Murad, E.: Differential ablation of cosmic dust and implications for the relative abundances of atmospheric metals, J. Geophys. Res., 103, 10899–10911, 1998. 4, 5

Mende, S. B., Swenson, G. R., and Miller, K. L.: Observations of E and F Region Mg^+ from Spacelab 1, J. Geophy. Res., 90, 6667–6673, 1985. 13

Minschwaner, K., Herceg, D., Budzien, S. A., Dymond, K. F., Fortna, C., and P., M. R.: Observations of middle ultraviolet emissions in the middle and lower thermosphere: NO, O_2, O and Mg^+, J. Geophys. Res., 112, A10311, 2007. 13, 14

Murad, E. and Williams, I. P.: Meteors in the Earth's atmosphere, Cambridge University Press, Cambridge, 2002. 4

Narcisi, R. S.: Composition studies of the lower ionosphere, in: Physics of the Upper Atmosphere, 11–59, 1971TS10. 12

Narcisi, R. S. and Bailey, A. D.: Mass spectrometric measurements of positive ions at altitudes from 64 to 112 kilometers, J. Geophys. Res., 70, 3687–3700, 1965. 12

Nesvorný, D., Jenniskens, P., Levison, H. F., Bottke, W., Vokrouhlický, D., and Gounelle, M.: Cometary origin of the Zodiacal Cloud and carbonaceous micrometeorites, implications for hot debris disks, Astrophys. J., 713, 816–836, 2010. 4

Nesvorný, D., Janches, D., Vokrouhlický, P., Pokorný, P., Bottke, W. F., and Jenniskens, P.: Dynamical model for the zodiacal cloud and sporadic meteors, Ap. J., 743, 129, 2011a. 4

Please note the remarks at the end of the manuscript.

ACPD
14, 1–49, 2014

Global investigation of the Mg atom and ion layers

M. Langowski et al.

Nesvorný, D., Vokrouhlický, P., Pokorný, P., and Janches, D.: Dynamics of dust particles released from oort cloud comets and their contribution to radar meteors, Ap. J., 743, 37, 2011b. 4

Philbrick, C. R., Narcisi, R. S., Good, R., Hoffmann, H. S., Keneshea, T. J., A., M. M., Zimmermann, S. P., and Reinisch, B. W.: The Aladdin Experiment – Part II, Composition, Space Res., VII, 441–449, 1973. 12

Plane, J. M. C.: Atmospheric chemistry of meteroric metals, Chem. Rev., 103, 4963–4984, 2003. 5

Plane, J. M. C.: Cosmic dust in the earth's atmosphere, J. Atmos. Sol.-Terr. Phy., 41, 6507–6518, 2012. 4

Plane, J. M. C. and Helmer, M.: Laboratory Study of Reactions $Mg + O_3$ and $MgO + O_3$, implications for the chemistry of magnesium in the upper atmosphere, Faraday Discuss., 100, 411–430, 1995. 5, 28, 29

Plane, J. M. C. and Whalley, C. L.: A new model for magnesium chemistry in the upper atmosphere, J. Phys. Chem. A, 116, 6240–6252, 2012. 5, 6, 16, 28, 29

Roddy, P. A., Earle, G. D., Swenson, C., Carlson, C. G., and Bullett, T. W.: Relative concentrations of molecular and metallic ions in the midlatitude intermediate and sporadic-E layers, Geophys. Res. Let., 31, L19807, 2004. 12

Rollason, R. J. and Plane, J. M. C.: A kinetic study of the reactions of MgO with H_2O, CO_2 and O_2: implications for magnesium chemistry in the mesosphere, Phys. Chem. Chem. Phys., 3, 4733–4740, 2001. 28, 29

Saunders, R. W. and Plane, J. M. C.: A laboratory study of meteor smoke analogues: composition, optical properties and growth kinetics, J. Atmos. Sol.-Terr. Phy., 68, 550–553, 2006. 5

Scharringhausen, M.: Investigation of Mesospheric and Thermospheric Magnesium Species from Space, Ph.D. thesis, 2007TS11. 6, 15

Scharringhausen, M., Aikin, A. C., Burrows, J. P., and Sinnhuber, M.: Space-borne measurements of mesospheric magnesium species – a retrieval algorithm and preliminary profiles, Atmos. Chem. Phys., 8, 1963–1983, doi:10.5194/acp-8-1963-2008, 2008a. 15

Scharringhausen, M., Aikin, A. C., Burrows, J. P., and Sinnhuber, M.: Global column density retrieval of mesospheric and thermospheric MgI and MgII from SCIAMACHY limb and radiance data, J. Geophys. Res., 113, D13303TS12, 2008b. 15

Please note the remarks at the end of the manuscript.

ACPD
14, 1–49, 2014

Global investigation of the Mg atom and ion layers

M. Langowski et al.

Swider, W.: Ionic and neutral concentrations of Mg and Fe near 92 km, Planet. Space Sci., 32, 307–312, 1984. 27

von Savigny, C., Kaiser, J. W., Bovensmann, H., Burrows, J. P., McDermid, I. S., and Leblanc, T.: Spatial and temporal characterization of SCIAMACHY limb pointing errors during the first three years of the mission, Atmos. Chem. Phys., 5, 2593–2602, doi:10.5194/acp-5-2593-2005, 2005. 13

von Savigny, C., Bovensmann, H., Bramstedt, K., Dikty, S., Ebojie, F., Jones, A., Noél, S., Rozanov, A., and Sinnhuber, B.-M.: Indications for long-term trends and seasonal variations in the SCIAMACHY Level 1 version 6.03 tangent height information, Techn. Note-IUP-scia-pointing-2009-01, University of Bremen, Bremen, Germany, Issue 2, 2009. 13

Vondrak, T., Plane, J. M. C., Broadley, S., and Janches, D.: A chemical model of meteoric ablation, Atmos. Chem. Phys., 8, 7015–7031, doi:10.5194/acp-8-7015-2008, 2008. 4, 5

Whalley, C. L. and Plane, J. M. C.: Meteoric ion layers in the Martian atmosphere, Faraday Discuss., 147, 349–368, 2010. 16, 28, 29

Zbinden, P. A., Hidalgo, M. A., Eberhardt, P., and Geiss, J.: Mass spectrometer measurements of the positive ion composition in the D- and E-Regions of the ionosphere, Planet. Space Sci., 23, 1621–1642, 1975. 12

ACPD
14, 1–49, 2014

Table 1. Magnesium Photolysis Chemistry added into WACCM.

No.	Reaction	Rate/s^{-1}	Reference
J1	$Mg + h\nu \rightarrow Mg^{+} + e^{-}$	$j_1 = 4 \times 10^{-7}$	Swider (1984)

ACPD
14, 1–49, 2014

Table 2. Neutral chemistry of magnesium added into WACCM.

No.	Reaction	Rate/cm^3 molecule^{-1} s^{-1}	Reference
R1	$Mg + O_3 \rightarrow MgO + O_2$	$k_1 = 2.3 \times 10^{-10} \exp(-139/T)$	Plane and Helmer (1995)
R2	$MgO + O \rightarrow Mg + O_2$	$k_2 = 6.2 \times 10^{-10} \times (T/295)^{0.167}$	Whalley and Plane (2010)
R3	$MgO + O_3 \rightarrow MgO_2 + O_2$	$k_3 = 2.2 \times 10^{-10} \exp(-548/T)$	Plane and Helmer (1995)
R4	$MgO_2 + O \rightarrow MgO + O_2$	$k_4 = 7.9 \times 10^{-11} \exp(T/295)^{0.167}$	Whalley and Plane (2010)
R5	$MgO + H_2O + M \rightarrow MgO_2H_2 + M$	$k_5 = 1.1 \times 10^{-26} \times (T/200)^{-1.59}$	Rollason and Plane (2001)
R6	$MgO_3 + H_2O \rightarrow MgO_2H_2 + O_2$	$k_6 = 1.0 \times 10^{-12}$	Rollason and Plane (2001)
R7	$MgO + O_2 + M \rightarrow MgO_3 + M$	$k_7 = 3.8 \times 10^{-29} \times (T/200)^{-1.59}$	Rollason and Plane (2001)
R8	$MgO + CO_2 + M \rightarrow MgCO_3 + M$	$k_8 = 5.9 \times 10^{-29} \times (T/200)^{-0.86}$	Rollason and Plane (2001)
R9	$MgCO_3 + O \rightarrow MgO_2 + CO_2$	$k_9 = 6.7 \times 10^{-12}$	Plane and Whalley (2012)
R10	$MgO_2 + O_2 + M \rightarrow MgO_4 + M$	$k_{10} = 1.8 \times 10^{-26} \times (T/200)^{-2.5}$	Plane and Whalley (2012)
R11	$MgO_4 + O \rightarrow MgO_3 + O_2$	$k_{11} = 8.0 \times 10^{-14}$	Plane and Whalley (2012)
R12	$MgO_2H_2 + H \rightarrow MgOH + H_2O$	$k_{12} = 1.0 \times 10^{-11} \times \exp(-600/T)$	Plane and Whalley (2012)
R12b	$MgOH + H \rightarrow Mg + H_2O$	faster than R12	see text
R13	$MgO_2H_2 + MgO_2H_2 \rightarrow (MgO_2H_2)_2$	$k_{13} = 9.0 \times 10^{-10}$	see text
R14	$MgO_3 + H \rightarrow MgOH + O_2$	$k_{14} = 2.0 \times 10^{-12}$	Plane and Whalley (2012)

ACPD
14, 1–49, 2014

Table 3. Ion-molecule chemistry of magnesium added into WACCM.

No.	Reaction	Rate/cm^3 molecule^{-1} s^{-1}	Reference
R15	$Mg^+ + O_3 \rightarrow MgO^+ + O_2$	$k_{15} = 1.2 \times 10^{-9}$	Whalley and Plane (2010)
R16	$MgO^+ + O \rightarrow Mg^+ + O_2$	$k_{16} = 5.9 \times 10^{-10}$	Whalley and Plane (2010)
R17	$MgO^+ + O_3 \rightarrow Mg^+ + 2O_2$	$k_{17} = 1.8 \times 10^{-10}$	Whalley and Plane (2010)
R18	$MgO^+ + O_3 \rightarrow MgO_2^+ + O_2$	$k_{18} = 3.3 \times 10^{-10}$	Whalley and Plane (2010)
R19	$Mg^+ + N_2 + M \rightarrow MgN_2{}^+ + M$	$k_{19} = 1.8 \times 10^{-30}(T/200)^{-1.72}$	Whalley and Plane (2010)
R20	$Mg^+ + O_2 + M \rightarrow MgN_2{}^+ + M$	$k_{20} = 2.4 \times 10^{-30}(T/200)^{-1.65}$	Whalley and Plane (2010)
R21	$MgN_2^+ + e \rightarrow Mg + N_2$	$k_{21} = 3.0 \times 10^{-7}(T/200)^{-0.5}$	Plane and Whalley (2012)
R22	$MgCO_2^+ + e \rightarrow Mg + CO_2$	$k_{22} = 3.0 \times 10^{-7}(T/200)^{-0.5}$	Plane and Whalley (2012)
R23	$MgH_2O^+ + e \rightarrow Mg + H_2O$	$k_{23} = 3.0 \times 10^{-7}(T/200)^{-0.5}$	Plane and Whalley (2012)
R24	$MgO^+ + e \rightarrow Mg + O$	$k_{24} = 3.0 \times 10^{-7}(T/200)^{-0.5}$	Plane and Whalley (2012)
R25	$Mg^+ + e^- \rightarrow Mg + h\nu$	$k_{25} = 1.0 \times 10^{-12}$	Plane and Helmer (1995)
R26	$Mg + O_2{}^+ \rightarrow Mg^+ + O_2$	$k_{26} = 1.2 \times 10^{-9}$	Anderson and Barth (1971)
R27	$Mg + N_2{}^+ \rightarrow Mg^+ + N_2$	$k_{27} = 8.2 \times 10^{-10}$	Anderson and Barth (1971)
R28	$MgN_2{}^+ + O_2 \rightarrow MgO_2{}^+ + N_2$	$k_{28} = 3.5 \times 10^{-12}$	Rollason and Plane (2001)
R29	$MgO_2{}^+ + O \rightarrow MgO^+ + O_2$	$k_{29} = 6.5 \times 10^{-10}$	Rollason and Plane (2001)
R30	$MgO^+ + O_3 \rightarrow Mg^+ + 2O_2$	$k_{30} = 1.8 \times 10^{-10}$	Whalley and Plane (2010)
R31	$Mg^+ + H_2O + M \rightarrow MgH_2O^+ + M$	$k_{31} = 2.3 \times 10^{-28}(T/200)^{-2.53}$	Martinez-Nunez et al. (2010)
R32	$Mg^+ + CO_2 + M \rightarrow MgCO_2{}^+ + M$	$k_{32} = 4.6 \times 10^{-29}(T/200)^{-1.42}$	Whalley and Plane (2010)

ACPD
14, 1–49, 2014

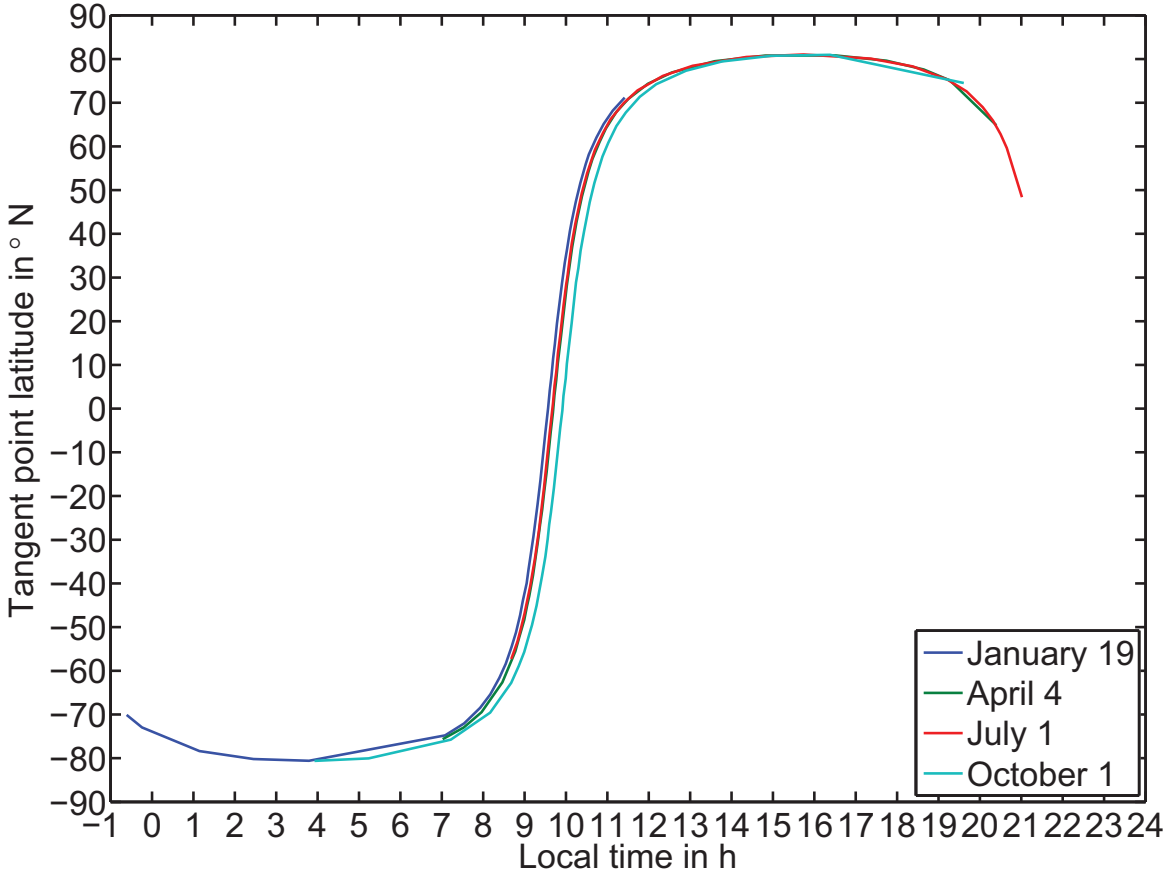

Fig. 1. Local time of SCIAMACHY measurements at different latitudes for different seasons of the year.

ACPD
14, 1–49, 2014

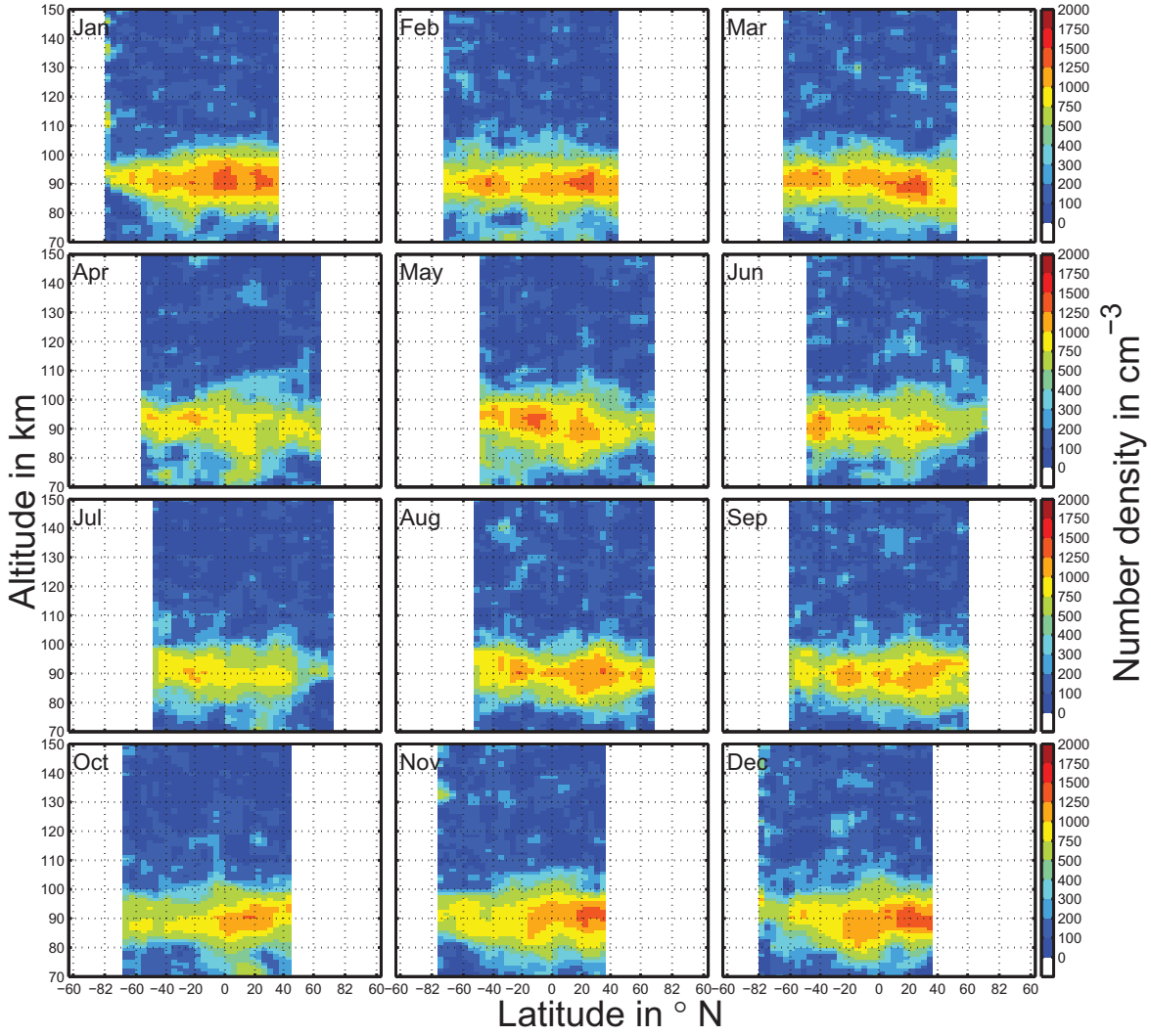

Fig. 2. Latitudinal variation of monthly (averaged over all January, February, etc. results from 2008–2012) and zonally averaged Mg density profiles retrieved from the 285.2 nm line. The Mg layer peaks around 90 km altitude and has a FWHM of about 15 km. Mg shows strong month-to-month variations, but there is no clear seasonal cycle to be observed.

ACPD
14, 1–49, 2014

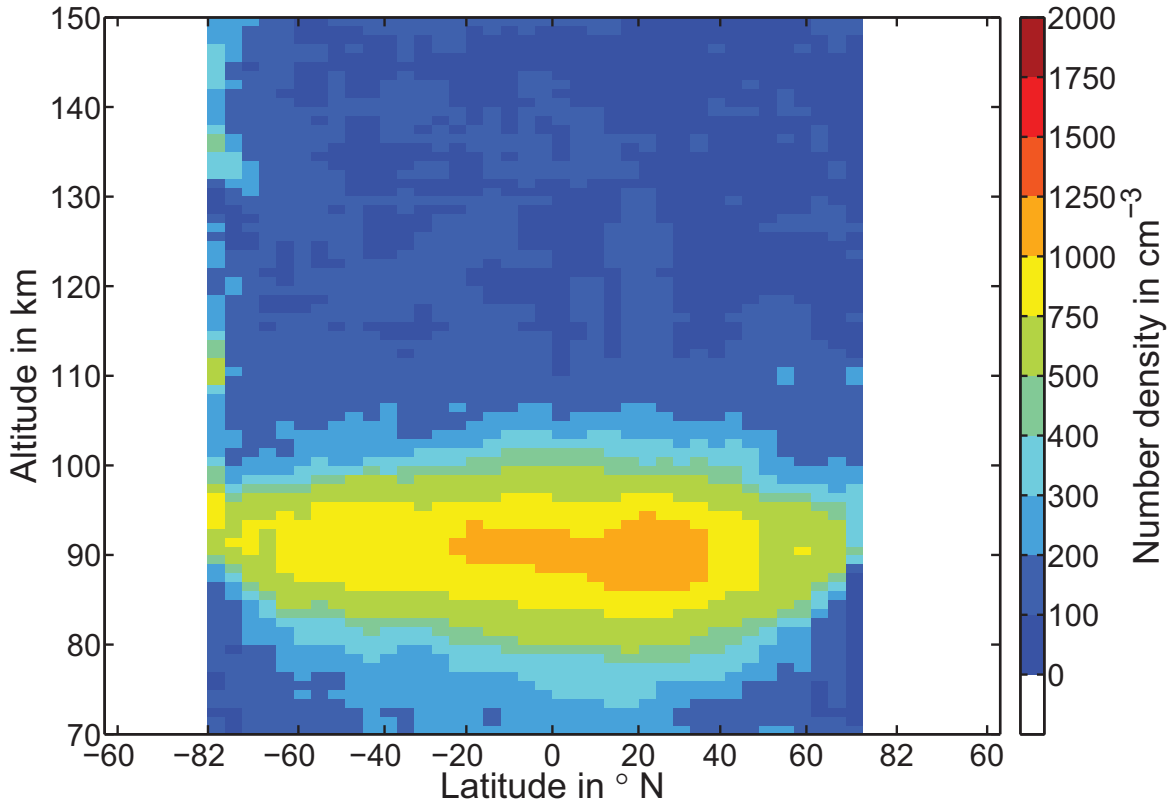

Fig. 3. Latitudinal variation of Mg profiles averaged over all available data for the years 2008–2012. Note that only between 45° N and S measurements from all 12 months contribute to the averages, while for high-latitudes there is only summer coverage and/or near-terminator measurements.

ACPD
14, 1–49, 2014

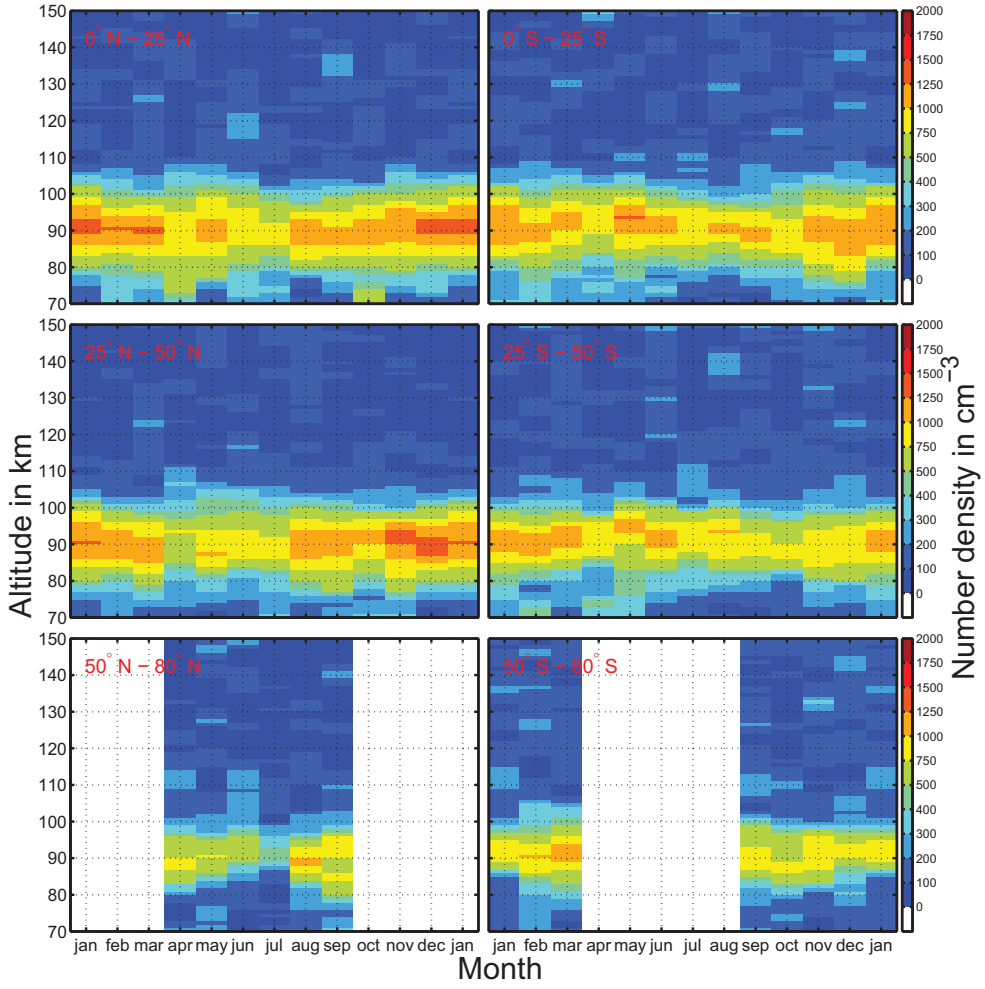

Fig. 4. Seasonal variation of the vertical Mg profile for different latitudinal zones (left: Northern Hemisphere, right: Southern Hemisphere, top: low-latitudes, mid: mid-latitudes, bottom: high-latitudes). The peak altitude is at 90 km for all latitudes with variations of ±5 km. The month-to-month variations in peak altitude and density are bigger than any seasonal variations.

ACPD
14, 1–49, 2014

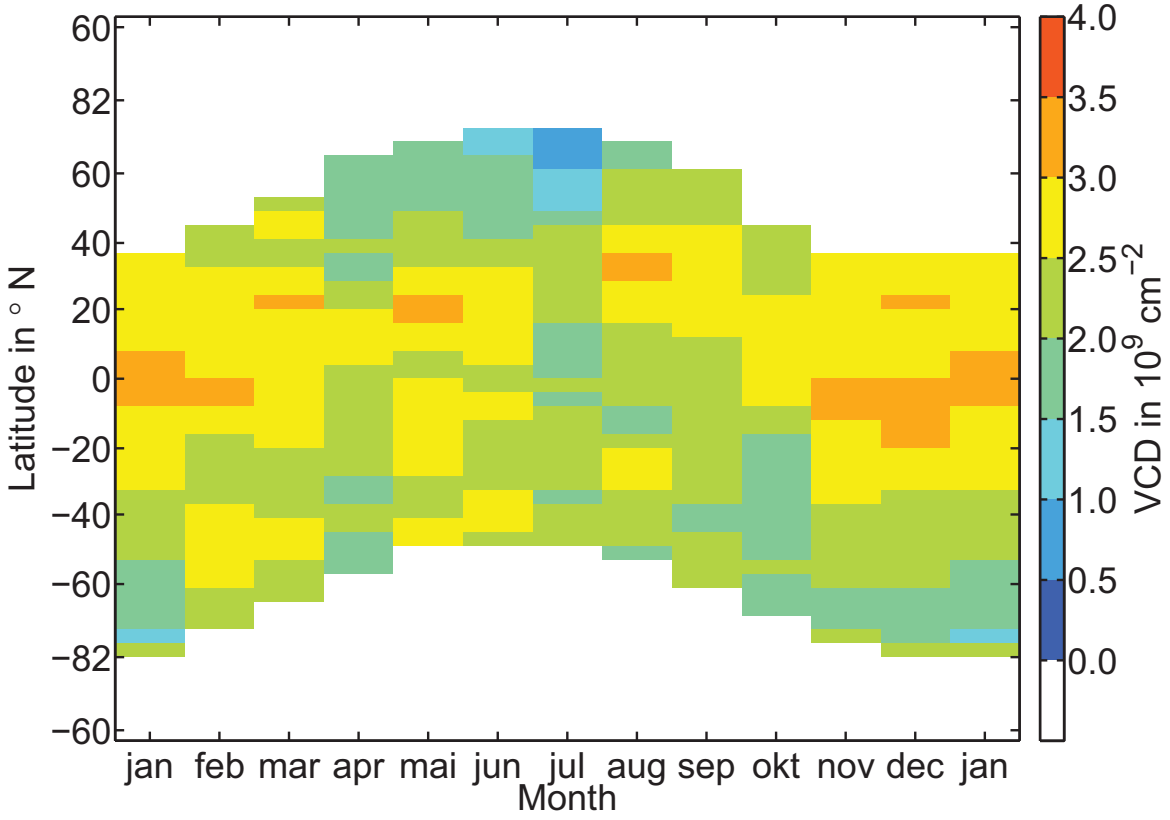

Fig. 5. Seasonal variation of the Mg vertical column density (VCD) between 70 km and 150 km for different latitudinal regions. The VCD varies between 0.5×10^9 cm^{-2} and 3.5×10^9 cm^{-2}. No clear seasonal cycle is observed. Variations between consecutive days with measurements (at least 14 days difference) are even higher than the inter-monthly variations.

ACPD
14, 1–49, 2014

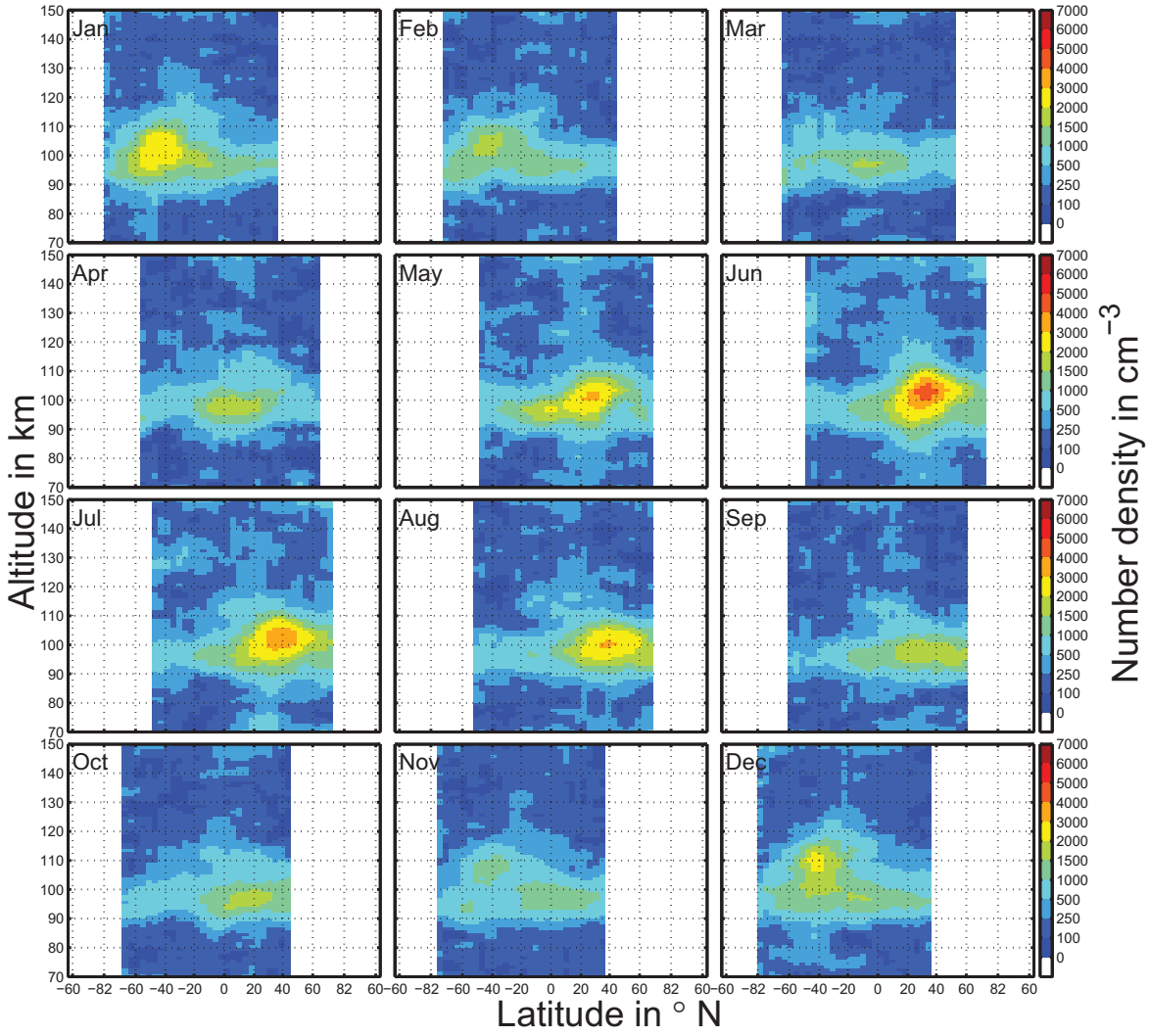

Fig. 6. Latitudinal variation of monthly and zonally averaged Mg^+ profiles (for the years 2008–2012) retrieved from the Mg^+ line at 279.6 nm. Mg^+ shows a seasonal cycle with a summer maximum, which is especially pronounced in the region between 25° and 45° latitude in the summer hemisphere. Furthermore, in this region the peak altitude is about 105 km, which is up to 10 km higher than at the equator or at the poles.

ACPD
14, 1–49, 2014

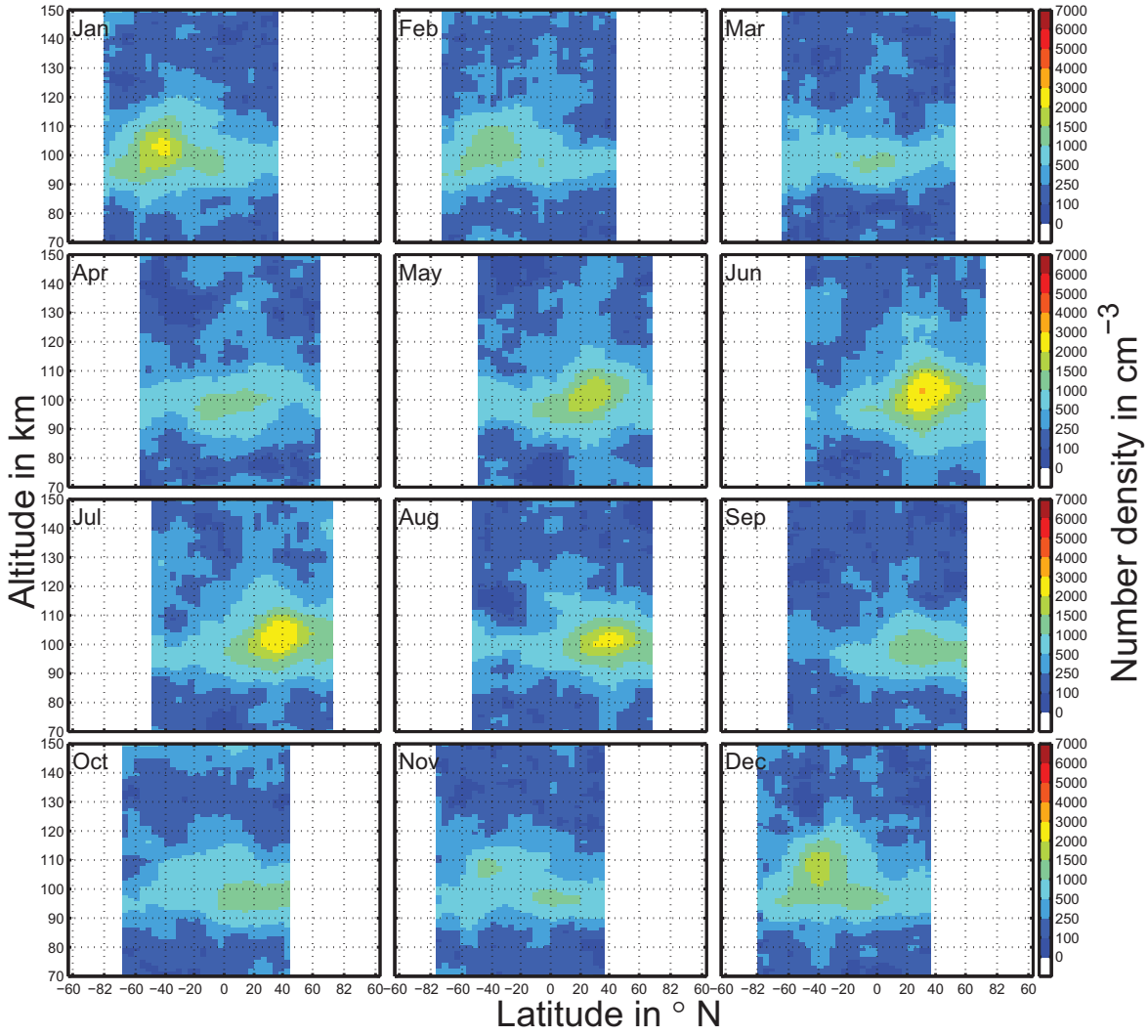

Fig. 7. Latitudinal variation of monthly and zonally averaged Mg^+ profiles (for the years 2008–2012) retrieved from the Mg^+ line at 280.4 nm. The results from the 280.4 nm line are in good agreement with the results based on the 279.6 nm line shown in Fig. 6. The 280.4 nm line retrievals show slightly higher densities above 110 km and a slightly smaller peak density, especially when the peak density is high. Note that the peak at 150 km and high northern latitude is probably an artifact of the retrieval.

ACPD
14, 1–49, 2014

Global investigation of the Mg atom and ion layers

M. Langowski et al.

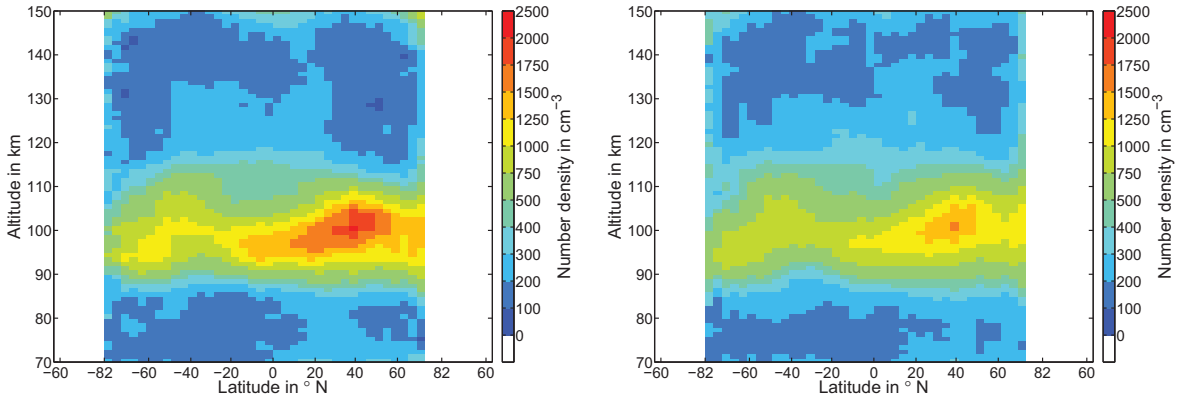

Fig. 8. Latitudinal variation of Mg^+ profiles averaged over all available data for 2008–2012 for the Mg^+ line at 279.6 nm (left) and the Mg^+ line at 280.4 nm (right). Results for both lines show an asymmetric behaviour between the Northern Hemisphere and the Southern Hemisphere with a more pronounced summer maximum in the Northern Hemisphere.

ACPD
14, 1–49, 2014

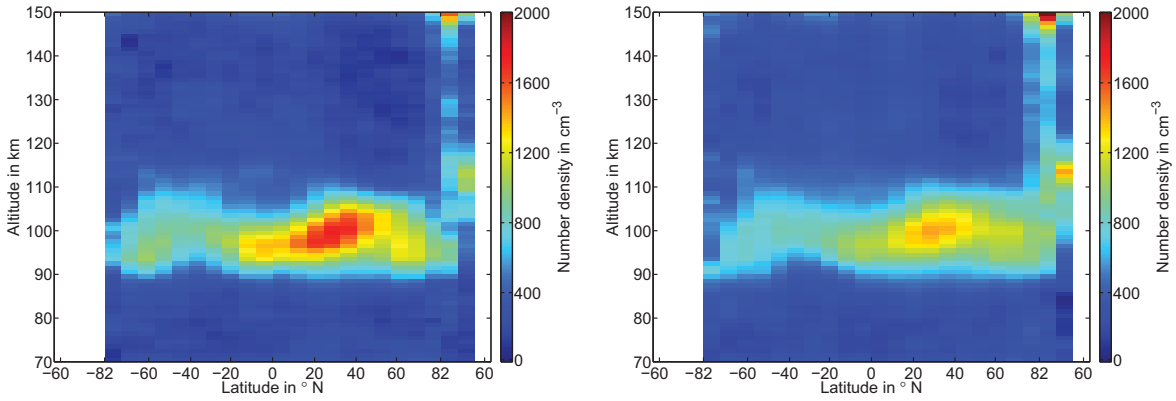

Fig. 9. Mg^+ profiles averaged over all available data for 2008–2012 for the Mg^+ line at 279.6 nm (left) and the Mg^+ line at 280.4 nm (right). The stray light contaminated measurements at the start of each orbit are also used here extending the coverage to higher northern latitudes and even the ascending node side. High Mg^+ densities are observed at the north pole.

ACPD
14, 1–49, 2014

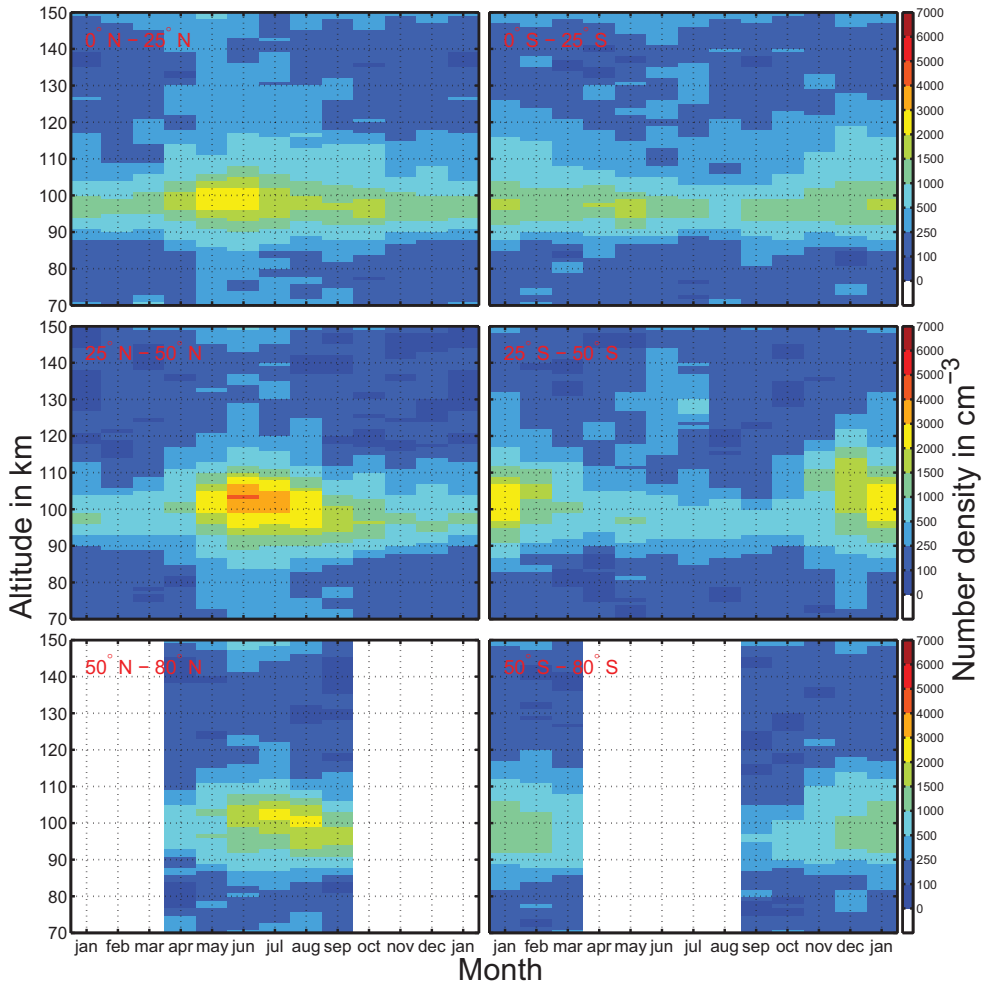

Fig. 10. Seasonal variation of the vertical profile of Mg^+ (279.6 nm line) for different latitudinal zones (left: Northern Hemisphere, right: Southern Hemisphere, top: low-latitudes, mid: mid-latitudes, bottom: high-latitudes), averaged over all available observations in 2008–2012. For all these latitudinal zones a seasonal cycle in the peak altitude with a summer maximum and a winter minimum can be observed. The seasonal variations are similar or larger than the month-to-month variations. The maximum peak altitude is 5–10 km higher than the minimum peak altitude. For mid-latitudes, the peak altitude in the winter hemisphere is still higher than the peak altitude at the equator (see also Fig. 6).

ACPD
14, 1–49, 2014

Global investigation of the Mg atom and ion layers

M. Langowski et al.

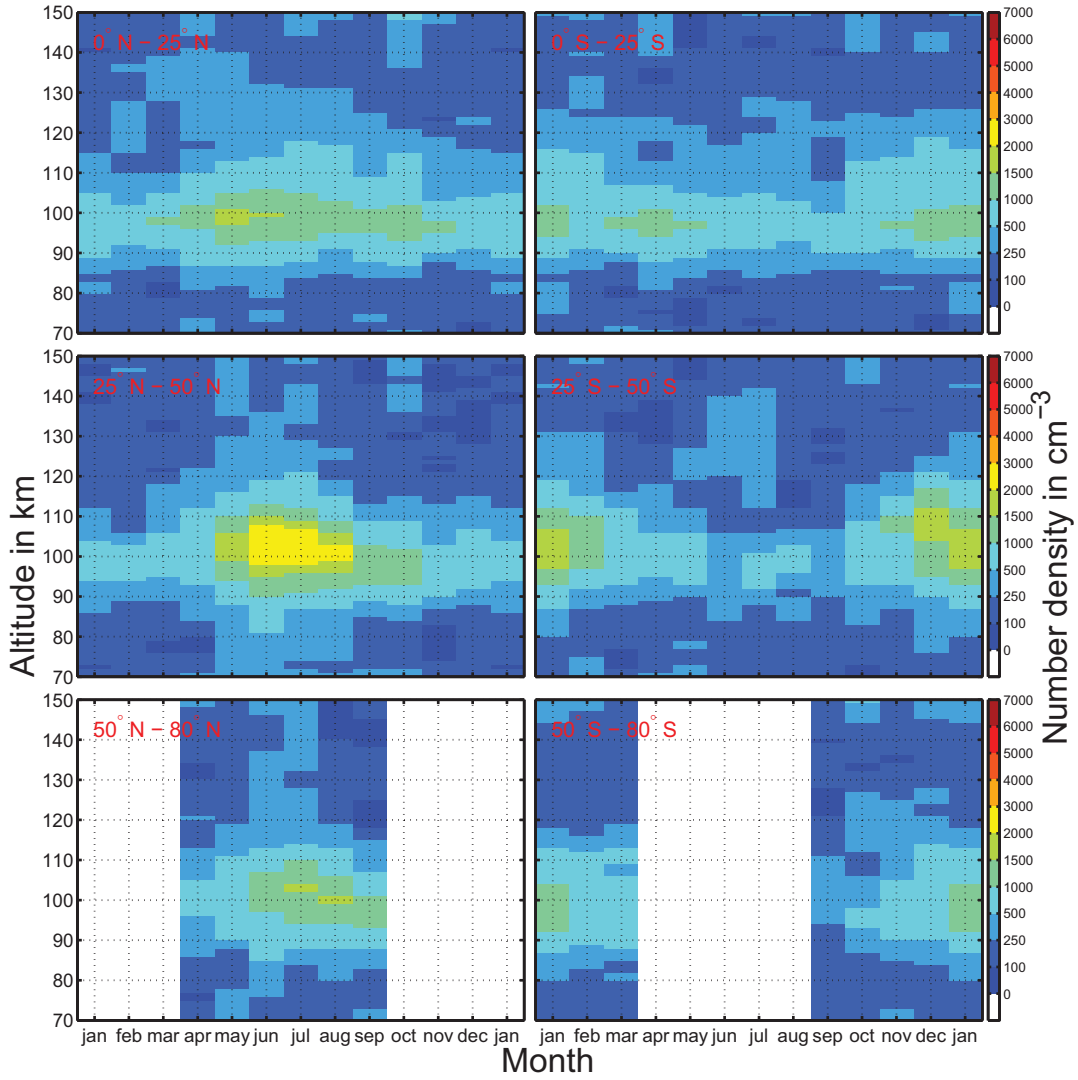

Fig. 11. Seasonal variation of the vertical profile of Mg^+ (280.4 nm line) for different latitudinal zones (left: Northern Hemisphere, right: Southern Hemisphere, top: low-latitudes, mid: mid-latitudes, bottom: high-latitudes), averaged over all available observations in 2008–2012. The results are in good agreement with the results in Fig. 10.

ACPD
14, 1–49, 2014

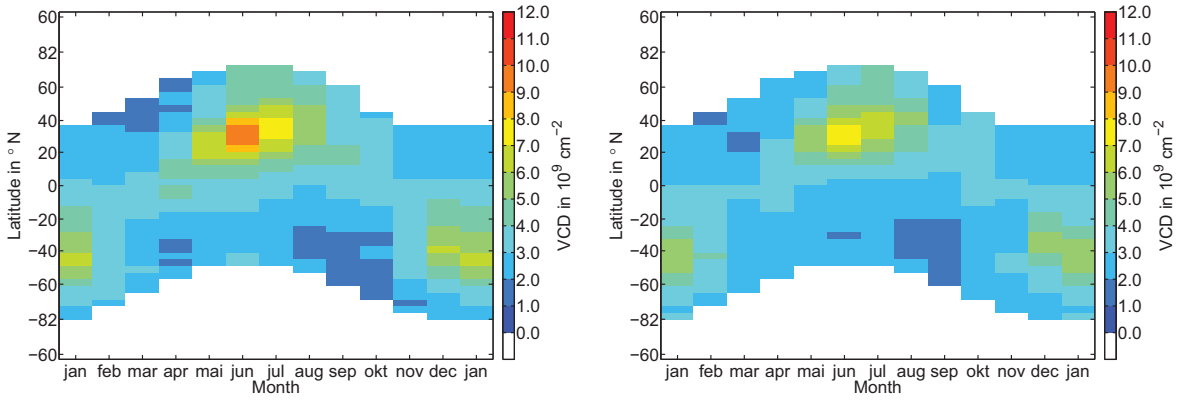

Fig. 12. Seasonal variation of the Mg^+ vertical column density (VCD) between 70 km and 150 km and for different latitudinal regions, retrieved from the 279.6 nm line (left) and the 280.4 nm line (right). A clear seasonal cycle with a summer maximum can be observed. The summer maximum in the Northern Hemisphere has higher values compared to the one in the Southern Hemisphere. The highest variability can be found between 25° and 50° in both hemispheres.

ACPD
14, 1–49, 2014

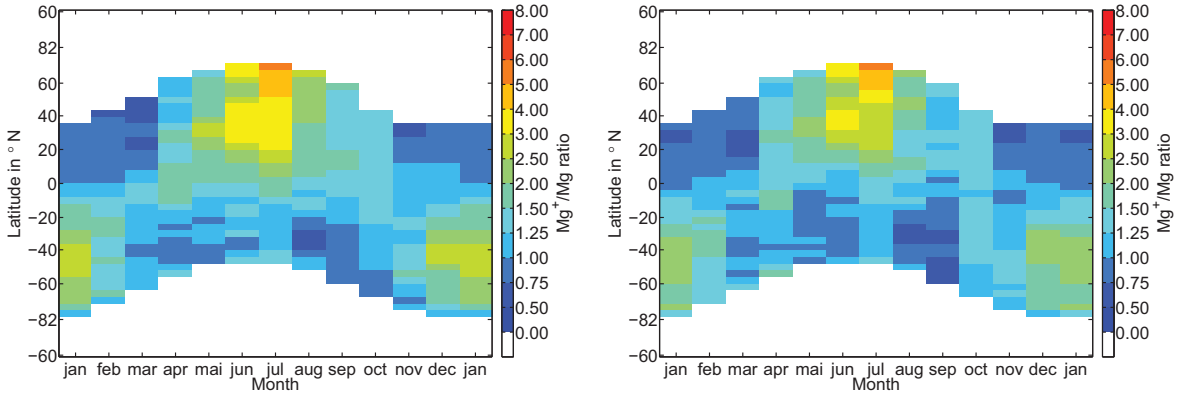

Fig. 13. Seasonal variation of the Mg^+ (left 279.6 nm, right 280.4 nm) to Mg ratio for different latitudes. At high northern latitudes the ratio may exceed the value of 6. For mid-latitudes the ratio varies between 0.5 and 4 and shows a summer maximum, which is in good agreement with Correira et al. (2008).

ACPD
14, 1–49, 2014

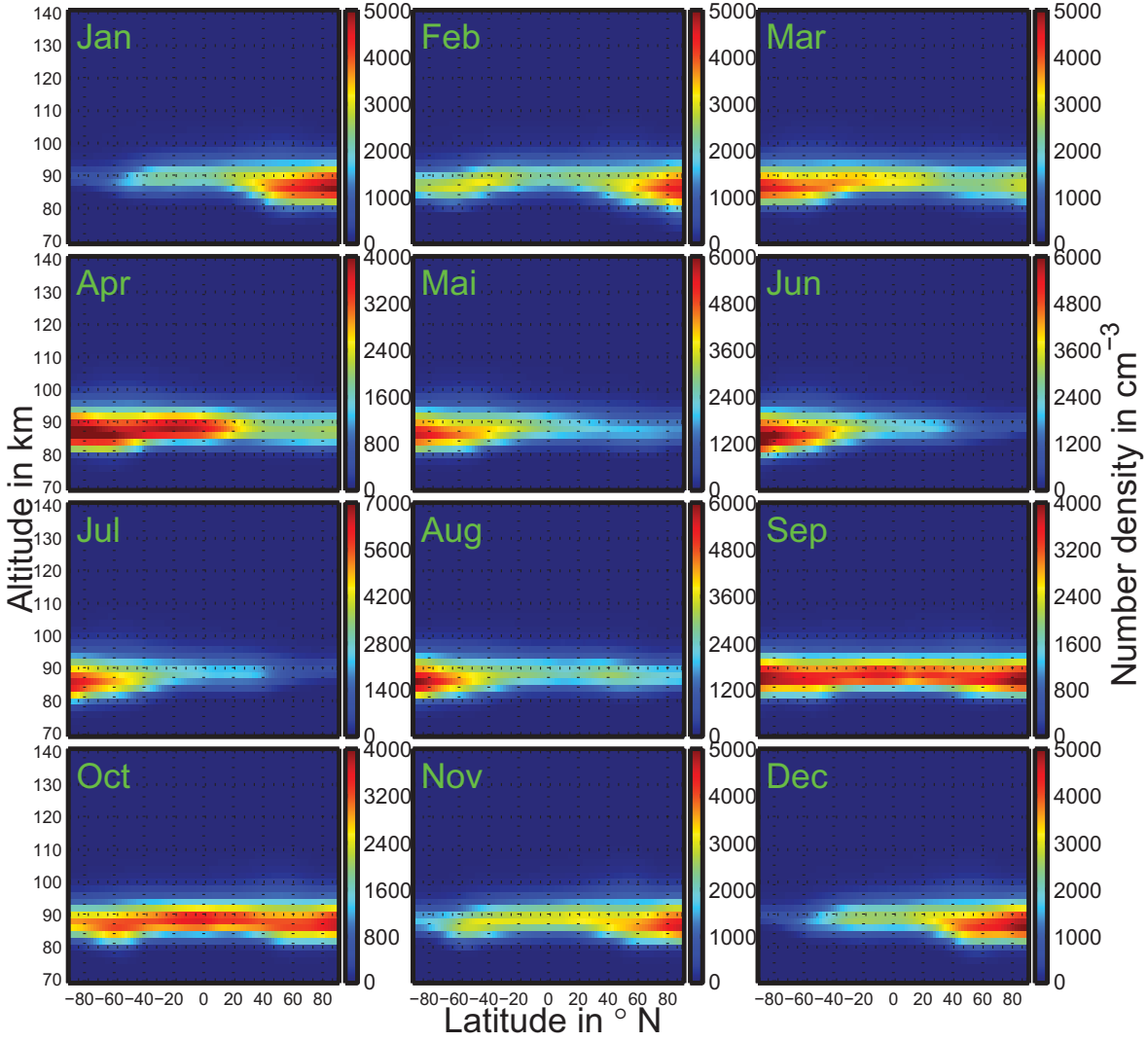

Fig. 14. Monthly mean WACCM results for Mg. The model results show a clear seasonal cycle with a winter maximum, most pronounced in the high-latitudes.

ACPD
14, 1–49, 2014

Global investigation of the Mg atom and ion layers

M. Langowski et al.

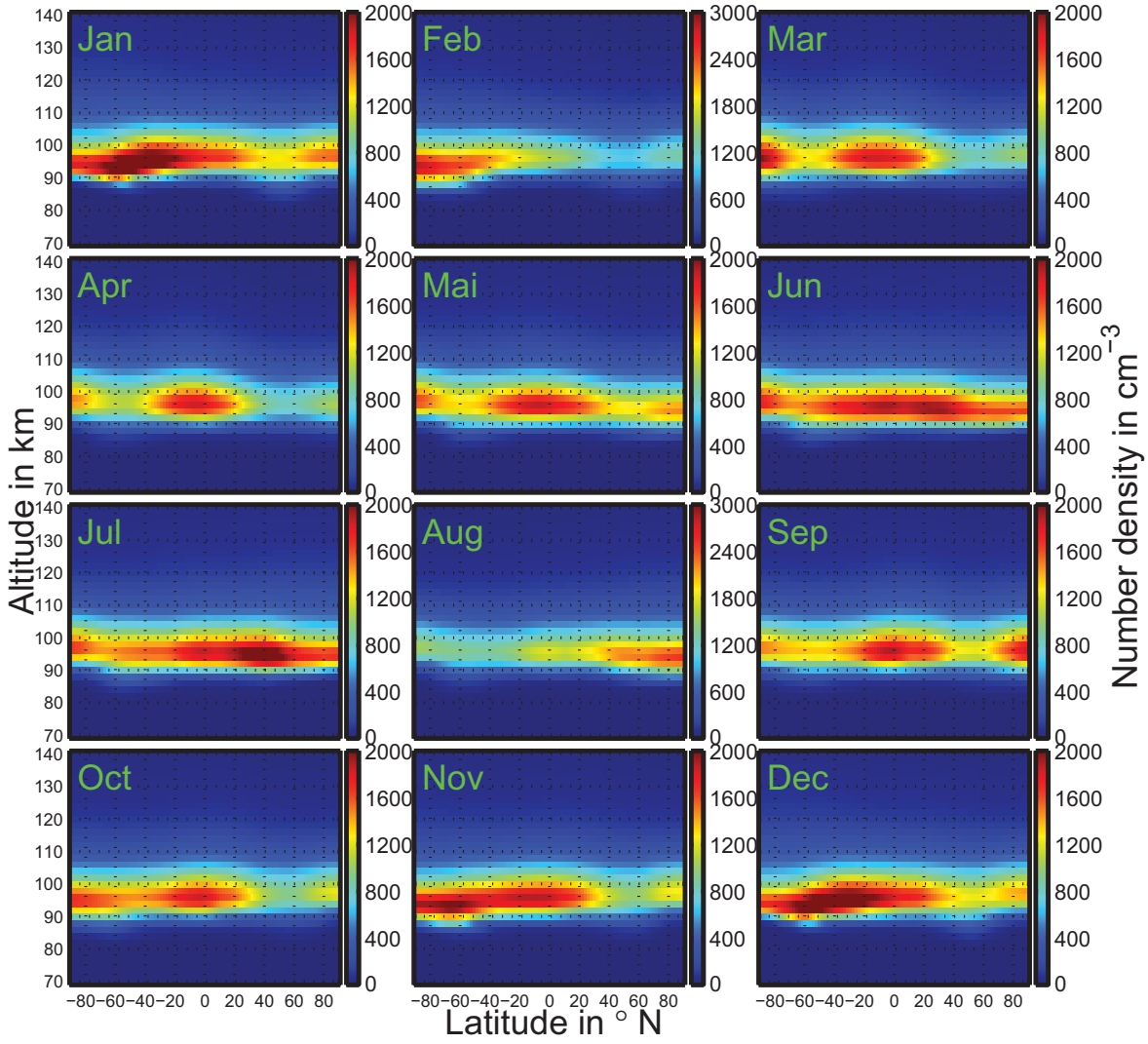

Fig. 15. Monthly mean WACCM results for Mg^+. The model results show a clear seasonal cycle with a summer maximum, most pronounced in the high-latitudes. There is also a second smaller maximum at high-latitudes for the winter hemisphere.

ACPD
14, 1–49, 2014

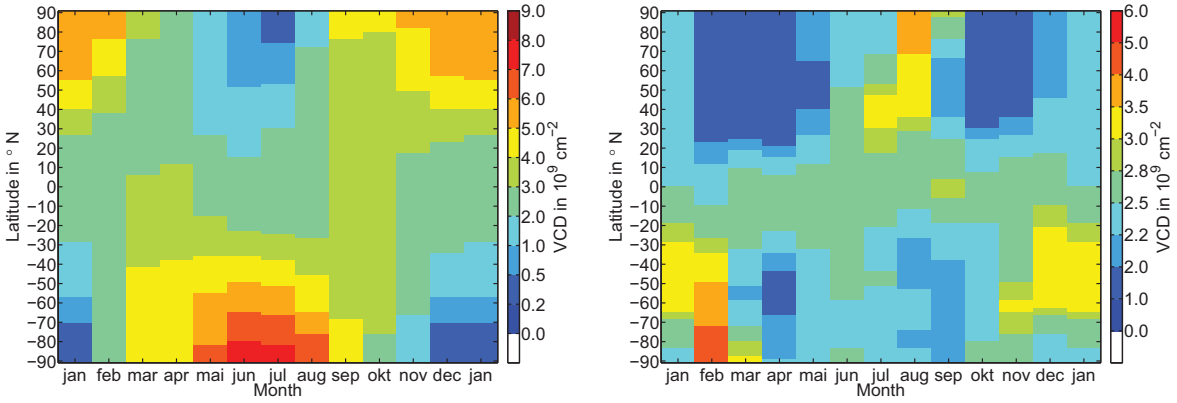

Fig. 16. VCD timelines for different latitudes for Mg (left) and Mg^+ (right). Mg VCDs vary between 0.5×10^9 cm^{-2} and 8×10^9 cm^{-2} and show a clear seasonal cycle with a winter maximum, which is most pronounced at the poles. Mg^+ VCDs vary from 1×10^9 cm^{-2} to 5×10^9 cm^{-2}, with most VCDs between 2×10^9 cm^{-2} and 3×10^9 cm^{-2}. A clear seasonal cycle with a summer maximum for Mg^+ is observed. SCIAMACHY results of VCDs are shown in Figs. 5 and 12.

ACPD
14, 1–49, 2014

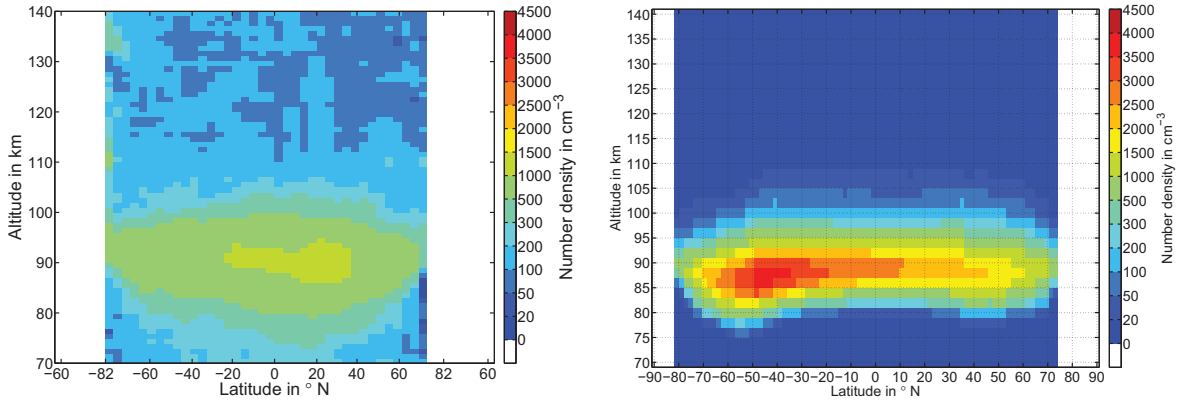

Fig. 17. Annual means of Mg for SCIAMACHY (left) and WACCM (right). SCIAMACHY shows (roughly a factor 2) smaller densities and a wider vertical profile. The averaging for WACCM considers only the time periods, where SCIAMACHY measurements are available.

ACPD
14, 1–49, 2014

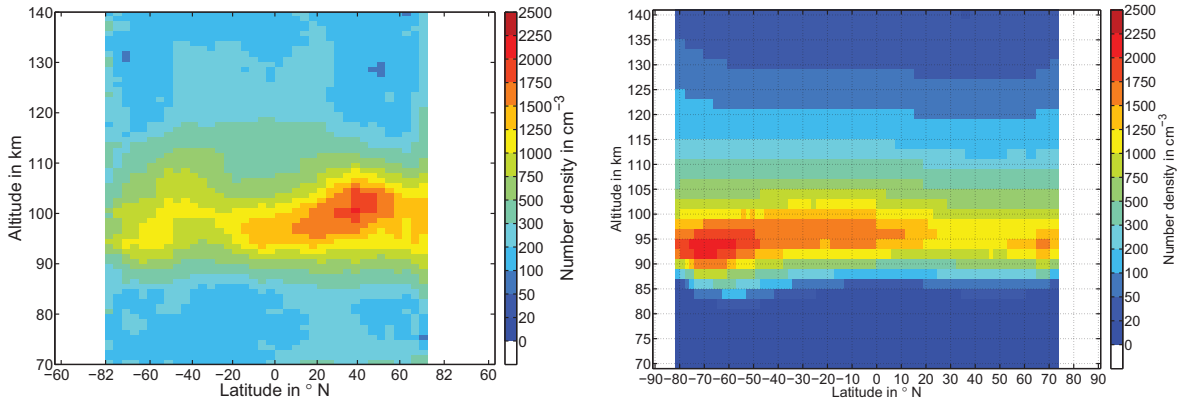

Fig. 18. Annual means of Mg^+ for SCIAMACHY (left, 279.6 nm) and WACCM (right). SCIAMACHY shows a wider vertical profile, and a stronger latitudinal dependence of the peak altitude. The peak densities are in very good agreement. The averaging for WACCM considers only the time periods, where SCIAMACHY measurements are available.

ACPD
14, 1–49, 2014

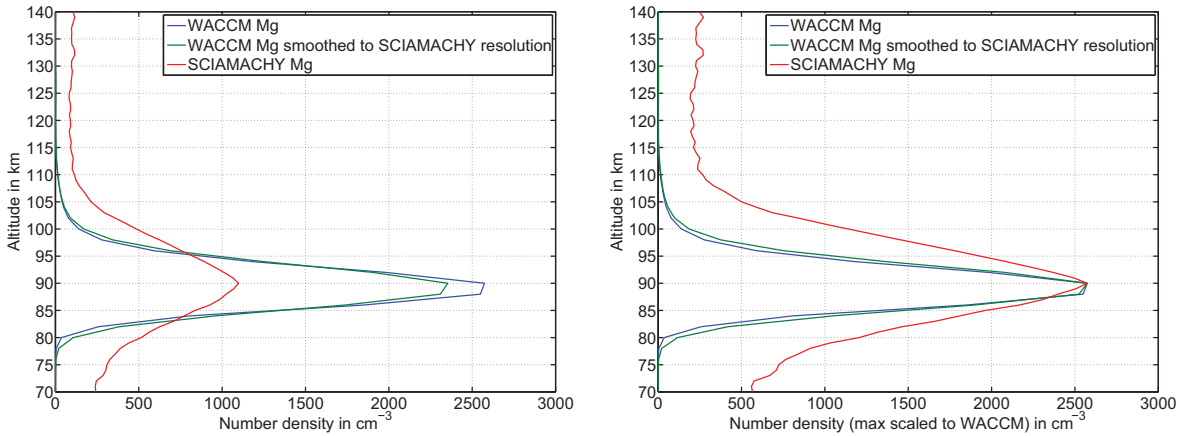

Fig. 19. Global annual mean vertical profile of Mg for SCIAMACHY and WACCM. The right plot shows the profiles normalized to the maximum of the WACCM profile, to better compare the shape of the profiles. The smoothed profile is smoothed with a triangular function with a base width of 4 km. The VCD between 70 and 140 km is 2.52×10^9 cm^{-2} for SCIAMACHY and 2.49×10^9 cm^{-2} for WACCM.

ACPD
14, 1–49, 2014

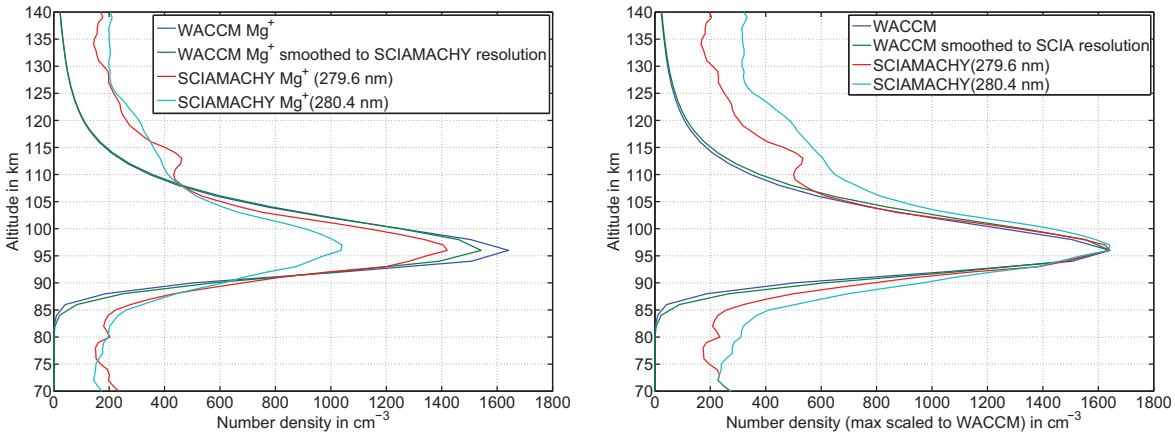

Fig. 20. Vertical profiles of Mg^+ for SCIAMACHY and WACCM at the equator. The right plot shows the profiles normalized to the maximum of the WACCM profile, to better compare the shape of the profiles. The profile shape for the 279.6 nm line matches the WACCM profile shape very well. The VCD between 70 and 140 km at the equator is 3.1×10^9 cm^{-2} and 2.8×10^9 cm^{-2} for SCIAMACHY (279.6/280.4 nm) and 2.4×10^9 cm^{-2} for WACCM.

ACPD
14, 1–49, 2014

Remarks from the Typesetter

TS1 Please provide place of publication and publisher.
TS2 Please provide DOI.
TS3 Please provide last access date.
TS4 Please provide DOI.
TS5 Please provide DOI.
TS6 Please provide DOI.
TS7 Please provide all author names.
TS8 Please provide place of publication and publisher.
TS9 Please provide page range or article number + DOI.
TS10 Please provide place of publication and publisher.
TS11 Please provide place of publication and publisher.
TS12 Please provide DOI.

ACPD
14, 1–49, 2014